

<sub>1</sub> Ammonium nitrate particles formed in upper  
<sub>2</sub> troposphere sourced from ground ammonia  
<sub>3</sub> during Asian monsoons

4 Michael Höpfner<sup>1</sup>, Jörn Ungermann<sup>2</sup>, Stephan Borrmann<sup>3,4</sup>, Robert  
5 Wagner<sup>1</sup>, Reinhold Spang<sup>2</sup>, Martin Riese<sup>2,5</sup>, Gabriele Stiller<sup>1</sup>, Oliver  
6 Appel<sup>3,4</sup>, Anneke M. Batenburg<sup>3,4</sup>, Silvia Bucci<sup>6</sup>, Francesco Cairo<sup>7</sup>, Antonis  
7 Dragoneas<sup>3,4</sup>, Felix Friedl-Vallon<sup>1</sup>, Andreas Hünig<sup>3,4</sup>, Sören Johansson<sup>1</sup>,  
8 Lukas Krasaukas<sup>2</sup>, Bernard Legras<sup>6</sup>, Thomas Leisner<sup>1</sup>, Christoph  
9 Mahnke<sup>3,4</sup>, Ottmar Möhler<sup>1</sup>, Sergej Molleker<sup>3,4</sup>, Rolf Müller<sup>2</sup>, Tom  
10 Neubert<sup>8</sup>, Johannes Orphal<sup>1</sup>, Peter Preusse<sup>2</sup>, Markus Rex<sup>9</sup>, Harald  
11 Saathoff<sup>1</sup>, Fred Stroh<sup>2</sup>, Ralf Weigel<sup>4</sup>, and Ingo Wohltmann<sup>9</sup>

12 <sup>1</sup>Institute of Meteorology and Climate Research, Karlsruhe Institute of  
13 Technology, Karlsruhe, Germany

14 <sup>2</sup>Institute of Energy and Climate Research, Stratosphere,  
15 Forschungszentrum Jülich, Jülich, Germany

16 <sup>3</sup>Department for Particle Chemistry, Max Planck Institute for Chemistry,  
17 Mainz, Germany

18 <sup>4</sup>Institute for Atmospheric Physics, Johannes Gutenberg University, Mainz,  
19 Germany

20 <sup>5</sup>Institute for Atmospheric and Environmental Research, University of  
21 Wuppertal, Wuppertal, Germany

22 <sup>6</sup>Laboratoire de Météorologie Dynamique, UMR8539, IPSL,  
23 CNRS/PSL-ENS/Sorbonne Université/École polytechnique, Paris, France

24 <sup>7</sup>Institute of Atmospheric Sciences and Climate, ISAC-CNR, Rome, Italy

25 <sup>8</sup>Central Institute of Engineering, Electronics and Analytics - Electronic  
26 Systems, Forschungszentrum Jülich, Jülich, Germany

27 <sup>9</sup>Alfred Wegener Institute, Helmholtz Center for Polar and Marine



29 The rise of ammonia emissions in Asia is predicted to increase  
30 radiative cooling and air pollution by forming ammonium nitrate  
31 particles in the lower troposphere. There is, however, a severe  
32 lack of knowledge about ammonia and ammoniated aerosol par-  
33 ticles in the upper troposphere and their possible effects on the  
34 formation of clouds. Here we employ satellite observations and  
35 high-altitude aircraft measurements, combined with atmospheric  
36 trajectory simulations and cloud-chamber experiments, to demon-  
37 strate the presence of ammonium nitrate particles and also track  
38 the source of ammonia forming into the particles. We find that  
39 solid ammonium nitrate particles are surprisingly ubiquitous in the  
40 upper troposphere from the Eastern Mediterranean to the West-  
41 ern Pacific during the Asian monsoon period – even as early as  
42 1997. We show that this ammonium nitrate aerosol layer is fed  
43 by convection that transports large amounts of ammonia from sur-  
44 face sources into the upper troposphere. Impurities of ammonium  
45 sulfate allow for the crystallization of ammonium nitrate even at  
46 conditions of high relative humidity prevailing in the upper tropo-  
47 sphere. Solid ammonium nitrate particles in the upper troposphere  
48 play a hitherto neglected role in ice cloud formation and the aerosol  
49 indirect radiative forcing.

50 Particulate ammonium nitrate (AN,  $\text{NH}_4\text{NO}_3$ ) and ammonium sulfate  
51 (AS,  $(\text{NH}_4)_2\text{SO}_4$ ) are important species in the tropospheric aerosol system.  
52 Ammonia ( $\text{NH}_3$ ), as the most abundant alkaline gas in the atmosphere, is  
53 the major precursor for the formation of these aerosols [1, 2]. Emissions  
54 of  $\text{NH}_3$  are estimated to keep rising over the coming decades [3, 4, 5, 6].  
55 Model calculations indicate that this will lead to an increase of the reflected  
56 solar radiation through AN particles, mainly produced in the lower part  
57 of the troposphere [7, 8]. At upper tropospheric levels, the presence of  $\text{NH}_3$   
58 may strongly enhance new particle formation through stabilization of sulfuric  
59 acid clusters especially at low temperatures prevalent at altitudes near the  
60 tropopause [9, 10]. Also in the upper troposphere (UT), solid AS particles  
61 were identified as potential ice nucleating particles affecting the formation  
62 and radiative properties of cirrus clouds [11]. Yet solid AS, as well as AN  
63 particles remain unobserved on a global scale in the UT. Furthermore, AN is  
64 generally assumed to exist as aqueous solution under UT conditions, so that  
65 it cannot promote heterogeneous ice formation [12, 13].

66 The presence of  $\text{NH}_3$  in the UT has recently been revealed by satellite  
67 observations during the Asian monsoon [14]. During that season, polluted air  
68 masses transported convectively from the boundary layer to high altitudes  
69 are confined in the so-called Asian summer Monsoon Anticyclone (AMA),  
70 e.g. [15]. In the AMA, pollution accumulates and is dispersed over a large  
71 area of the northern hemisphere reaching longitudes of 10–140°E and lati-  
72 tudes from 10–40°N [16, 17, 18, 19, 20, 21]. Air, which is exported from the  
73 AMA, influences the composition of the entire northern hemisphere lower-  
74 most stratosphere in summer [22, 23].

75 Connected to the AMA, a layer of enhanced aerosol loading at altitudes  
76 of 14–18 km was observed by satellite [24, 25, 26], and balloon-borne instru-  
77 ments [27]. Although little is known about the composition of the aerosol  
78 particles forming this Asian Tropopause Aerosol Layer (ATAL), its particles  
79 are currently believed to consist of carbonaceous and sulfate material and  
80 mineral dust [28, 29, 30, 31] or nitrate [32]. The ATAL particles are often  
81 connected with the presence of pollution markers in the monsoon circula-  
82 tion and large SO<sub>2</sub> emissions in South East Asia [26, 27]. Observations of  
83 the composition of ATAL aerosol particles are, however, sparse. Preliminary  
84 data from two single balloon flights indicate a presence of nitrate aerosol  
85 particles [27].

## 86 **Solid AN discovered by satellite and labora-** 87 **tory measurements**

88 The first evidence of solid AN aerosol particles in the UT is provided by  
89 satellite observations with the CRISTA (CRyogenic Infrared Spectrometers  
90 and Telescopes for the Atmosphere) instrument inside the AMA in August  
91 1997. We identified a distinct spectral signature at 831 cm<sup>-1</sup> that is only  
92 present in spectra taken inside the AMA as the  $\nu_2(\text{NO}_3^-)$  band of solid AN  
93 (Methods, Supplementary Fig. 1) [33]. Neither aqueous AN, nor any other  
94 aerosol or trace gas could replicate the observed spectral feature.

95 We investigated the crystallization behaviour of aqueous AN aerosol par-  
96 ticles at temperature conditions of the UT by AIDA (Aerosol Interaction and

97 Dynamics in the Atmosphere) aerosol and cloud chamber measurements. In  
98 agreement with previous studies that extended down to a temperature of  
99  $-35^{\circ}\text{C}$  [12], we did not detect the efflorescence of pure aqueous AN aerosol  
100 particles. However, the formation of solid AN was observed for particles  
101 composed of aqueous mixtures of AN and AS. At  $-50^{\circ}\text{C}$ , already a mole frac-  
102 tion of 2.9 mol% AS was sufficient to initiate the crystallization of AN. The  
103 crystallization rate was dependent on the ambient relative humidity (RH)  
104 with respect to supercooled liquid water. On a timescale of several hours,  
105 the formation of solid AN particles was even observed at RHs as high as  
106 61%, corresponding to an almost ice-saturated environment at  $-50^{\circ}\text{C}$  (Meth-  
107 ods and Supplementary Information). By demonstrating that small amounts  
108 of sulfate facilitate the formation of solid AN even at high RH, these exper-  
109 imental results strongly support the satellite detection of solid AN particles  
110 within the AMA. Further, the highly resolved laboratory infrared spectra  
111 of the  $\nu_2(\text{NO}_3^-)$  absorption band at low temperature provide the basis for a  
112 quantitative retrieval of AN particle mass density distributions from satellite  
113 and airborne observations (Methods).

114 The spatially resolved AN observations with the CRISTA satellite reveal  
115 that enhanced concentrations of AN ( $0.05\text{--}0.3\ \mu\text{g m}^{-3}$ ) are located only within  
116 the AMA (Fig. 1). These observations between 8 and 16 August 1997 indicate  
117 that an ATAL was present in the Asian monsoon UT in summer 1997, years  
118 earlier than hitherto thought [25].

119 The seasonal and inter-annual variability of AN concentrations in the  
120 AMA between 2002 and 2011 has been derived by analysis of spaceborne  
121 MIPAS (Michelson Interferometer for Passive Atmospheric Sounding) ob-

122 servations (Methods). Enhanced levels of AN appear in the second half of  
123 June, increase in areal coverage and concentration until mid-end of August,  
124 and reach values comparable to those derived from the CRISTA instrument  
125 (Fig. 2a). During these periods, the maximum concentrations are always  
126 located within the confines of the AMA, e.g. reaching as far as the Eastern  
127 Mediterranean (Supplementary Figs. 5, 6). This seasonal cycle is modulated  
128 by a large inter-annual variability with a clear maximum in 2008 with values  
129 three to four times higher than during other years.

130 Simultaneously observed concentrations of  $\text{NH}_3$  from a new MIPAS dataset  
131 (Methods) start to increase by mid-end of June, reach a maximum by mid-  
132 end of July and vanish until end of August (Fig. 2b and Supplementary  
133 Figs. 5, 6). This temporal evolution indicates a delay of 1–2 weeks of the AN  
134 maximum with respect to  $\text{NH}_3$ . This is consistent with the notion of advec-  
135 tive upward transport in the monsoon anticyclone at potential temperatures  
136 above about 360 K, which is much slower than convection [34]. In spite of  
137 this delay, the onset of enhanced values of AN and  $\text{NH}_3$  inside the AMA  
138 appears simultaneously by end of June.

## 139 **AN particles observed from aircraft in upper** 140 **troposphere**

141 High-altitude aircraft flights from Kathmandu, Nepal in July and August  
142 2017 within the StratoClim project (<http://www.stratoclim.org/>) pro-  
143 vided the first opportunity to measure the distribution and composition of



144 aerosols and trace gases inside the Asian monsoon UT with a variety of in situ  
145 and remote sounding instruments. Altitude profiles of AN and NH<sub>3</sub> along  
146 the flight track with a greatly improved resolution compared to the satel-  
147 lite products have been obtained from infrared limb-imaging observations  
148 with the airborne GLORIA (Gimballed Limb Observer for Radiance Imag-  
149 ing of the Atmosphere) instrument (Methods) [35, 36]. Figure 3 presents  
150 cross-sections of AN and NH<sub>3</sub> along the flight track on 31 July 2017 lead-  
151 ing from Kathmandu (27.7°N, 85.4°E) southwest-bound to about 21°N, 79°E  
152 and back. Due to the limb-sounding instrument’s observational direction to  
153 the right of the aircraft, the GLORIA measurements sampled air-masses of  
154 different origin during the SW-bound and NE-bound flight legs. During the  
155 SW-bound flight leg, we observed enhanced concentrations of AN aerosol  
156 mass reaching up to  $0.7 \mu\text{g m}^{-3}$  at around 16–17 km altitude (Fig. 3a,b). The  
157 height of this layer coincides with the typical altitude of the ATAL [26] and  
158 with our satellite retrievals. During the first part of the flight, a lower region  
159 of enhanced AN concentrations of up to  $0.5 \mu\text{g m}^{-3}$  between 12 km and 15 km  
160 altitude has been observed.

161 Distinct layers of enhanced values of total aerosol volume density are also  
162 observed by in-situ particle size distribution measurements during the ascent  
163 and descent of the aircraft on 31 July 2017 (Fig. 4a) [37, 38] (Methods).  
164 These correlate very well with maxima in the nitrate mass concentration  
165 profiles as measured by a flash vaporization/continuous ionization aerosol  
166 mass spectrometer (ERICA-AMS) [39, 40, 41] (Methods) (Fig. 4b). Though  
167 there is no exact coincidence between remote sensing and in situ measure-  
168 ments, the aerosol layer in the upper part of the profiles above about 15 km

169 is present in both kind of observations, as well as a second layer below. The  
170 retrieved values of nitrate aerosol mass concentration of around  $0.3 \mu\text{g m}^{-3}$   
171 from the infrared sounder fit to the independent in situ observations by the  
172 mass spectrometer (Supplementary Fig. 7).

173 Assuming the particle mass density of AN ( $1.72 \text{ g cm}^{-3}$ ) for conversion  
174 of the observed aerosol volume densities to  $\text{NO}_3^-$  mass concentrations, the  
175 resulting maximum values at 13–14 and 16 km agree with the mass spectro-  
176 metric data within the error margins. Thus, the hypothesis that a major  
177 fraction of the ATAL particle mass consists of AN is consistent with the  
178 observed aerosol volume densities at peak  $\text{NO}_3^-$  mass concentrations.

179 Additionally, the aerosol mass spectrometer detected the simultaneous  
180 presence of sulfate and nitrate in the mass spectra of individual single par-  
181 ticles (Methods, Supplementary Fig. 9). Such common occurrence of both  
182 components was observed in more than 91% of the particles analysed between  
183 10 and 17 km during the flight of 31 July 2017. These findings corroborate the  
184 results from the cloud-chamber observations on the crystallization behaviour  
185 of aqueous AS/AN mixtures.

## 186 **Ground $\text{NH}_3$ as the source of upper tropo-** 187 **spheric AN particles**

188 The region of enhanced AN at 12–15 km altitude during the first part of  
189 the flight (Fig. 3a, b) frames a zone of maximum concentrations of  $\text{NH}_3$   
190 (Fig. 3c, d). In this region,  $\text{NH}_3$  volume mixing ratios reach values of 1 ppbv

191 at 13.5 km altitude. During the previous flight, on 29 July 2017, NH<sub>3</sub> mixing  
192 ratios of even 1.4 ppbv have been encountered at similar altitudes. These  
193 concentrations are up to 40 times higher than the values reported previously  
194 [14], and are, thus, by far the highest concentrations of NH<sub>3</sub> ever observed  
195 in the UT.

196 High AN mass concentrations observed closely to the region of enhanced  
197 mixing ratios of NH<sub>3</sub> might either be due to similar source regions or by  
198 newly formed AN particles through gas to particle conversion within the  
199 plume of elevated NH<sub>3</sub> concentrations. Conversion of NH<sub>3</sub> volume mixing  
200 ratios to equivalent AN mass concentrations leads to maximum values of  
201 up to 1  $\mu\text{g m}^{-3}$ . Thus, the GLORIA measurements of that particular day  
202 show sufficiently high values of the gas phase NH<sub>3</sub> mixing ratios to explain  
203 concentrations up to 0.7  $\mu\text{g m}^{-3}$  of AN.

204 We have studied the possible origin of the elevated NH<sub>3</sub> concentrations in  
205 the UT by trajectory analyses in combination with satellite data of total col-  
206 umn amounts of NH<sub>3</sub> [42] (Methods, Supplementary Figs. 10 and 11). During  
207 the days prior to our aircraft measurements, enhanced column amounts of  
208 NH<sub>3</sub> have been observed at lower atmospheric levels in the region of NW-  
209 India and NE-Pakistan, a region known as a hot-spot for NH<sub>3</sub> emissions  
210 [6, 43, 44]. Trajectory simulations suggest that the high amounts of NH<sub>3</sub>  
211 observed by the GLORIA instrument have initially been transported con-  
212 vectively to altitudes of 12–14 km. Subsequently, they were advected by the  
213 anticyclonic upper tropospheric monsoon circulation to the location of the  
214 airborne observations within a few days. These measurements prove that  
215 NH<sub>3</sub> reaches the UT in amounts sufficient to explain the mass density of AN

216 observed. The relevant processes reducing the impact of washout of  $\text{NH}_3$   
217 during convection might involve low acidity of convective rain droplets [45],  
218 or a release of  $\text{NH}_3$  during the freezing process of cloud particles [46, 47, 48].

219 We uncover that a considerable part of the aerosol particles in the AMA  
220 consists of solid AN being formed through convective uplift of  $\text{NH}_3$  from  
221 intense surface emissions. Due to its longer lifetime, AN is subsequently  
222 transported vertically and horizontally inside the AMA, thereby already in-  
223 fluencing a large area of the northern hemisphere. Air masses with enhanced  
224 AN are not confined within the AMA but are transported either into the  
225 lowermost stratosphere at mid-latitudes or into the tropical belt. Here, due  
226 to dilution, the AN concentrations are no longer visible in our satellite data.  
227 It is highly probable that in the UT, these solid particles act as effective ice  
228 nucleating particles as has previously been demonstrated for solid AS [11].

229 In the future, rising emissions of  $\text{NH}_3$  will probably lead to a change  
230 of AN particles also in the UT with potential consequences for the Earth's  
231 radiative budget. For quantitative assessments using chemical-dynamical  
232 models, a better quantification of the  $\text{NH}_3$  surface emissions over the Indian  
233 sub-continent as well as a deeper understanding of the interaction processes  
234 of  $\text{NH}_3$  with liquid water and ice during convection is needed. Furthermore,  
235 it is most important to characterize the ice nucleating capacity of solid AN  
236 particles.

## 237 **Methods**

### 238 **Cloud chamber observations**

239 The AIDA aerosol and cloud chamber is a highly instrumented, 84.5 m<sup>3</sup>-  
240 sized aluminium vessel that can be operated at temperatures between +60  
241 and -90°C [49]. The ambient relative humidity can be controlled by evap-  
242 orating a specified amount of water vapour into the chamber. The number  
243 concentration and size distribution of aerosol particles added to the chamber  
244 are measured with a condensation particle counter (CPC, model 3010, TSI),  
245 a scanning mobility particle sizer (SMPS, model 3071A, TSI), and an aero-  
246 dynamic particle spectrometer (APS, model 3321, TSI). Relative humidity  
247 is measured in situ by tunable diode laser (TDL) absorption spectroscopy,  
248 detecting a rotational-vibrational water vapour absorption line at 1.37  $\mu\text{m}$   
249 [50]. Infrared extinction spectra of the aerosol particles are recorded in situ  
250 with a FTIR spectrometer (model IFS66v, Bruker) coupled to a multiple re-  
251 flection cell (optical path length 166.8 m, wavenumber range 6000–800 cm<sup>-1</sup>,  
252 0.5 cm<sup>-1</sup> resolution) [51]. With polarization-resolved in situ laser light scat-  
253 tering measurements, the backscattering linear depolarization ratio of the  
254 aerosol particles at a scattering angle of 178° and a wavelength of 488 nm  
255 are determined [52]. Due to the different infrared spectral signatures of liq-  
256 uid and solid AN, as well as the different depolarization levels of spherical,  
257 aqueous AN solution droplets and aspherical, crystalline AN particles, both  
258 the infrared and depolarization measurements allow for studying the phase  
259 change behaviour of the added aerosol particles. A schematic of the AIDA  
260 facility and further details about its optical instrumentation can be found in

261 [53].

262 For our experiments, the AIDA chamber was held at  $-50^{\circ}\text{C}$  and two dif-  
263 ferent relative humidities with respect to supercooled water, i.e., at 22% and  
264 61% RH, in order to simulate dry and humid upper tropospheric air masses.  
265 The aerosol particles were generated from aqueous solutions of 100 mol% AN,  
266 90 mol% AN + 10 mol% AS, and 97.1 mol% AN + 2.9 mol% AS. The bulk  
267 solutions were prepared by dissolving the respective chemicals (AN, VWR  
268 Chemicals, 99%; AS, Merck, 99.5%) in high purity water (GenPure Pro UV  
269 ultrapure water system, Thermo Scientific), using an overall solute concentra-  
270 tion of 10 wt%. Aqueous solution droplets were produced with an ultrasonic  
271 nebulizer (GA 2400, SinapTec). The aerosol flow first passed a set of sil-  
272 ica gel diffusion dryers (Topas GmbH) to reduce the RH in the aerosol flow  
273 to  $\leq 3\%$  and was then injected into the AIDA chamber through a stainless  
274 steel tube. The spectrum of liquid AN shown in Supplementary Fig. 1 was  
275 recorded after injection of the 100 mol% AN solution into the AIDA chamber  
276 at 61% RH, whereas the spectrum of the crystalline phase was recorded for  
277 the 97.1 mol% AN + 2.9 mol% AS mixture at 22% RH. Pertinent details of  
278 these experiments are further discussed in the Supplementary Information.

279 In order to derive mass-specific absorption coefficients of the recorded  
280  $\nu_2(\text{NO}_3^-)$  infrared absorption band of crystalline AN (Supplementary Fig. 1),  
281 which were then used as input for the aerosol mass density retrievals from  
282 the satellite observations, we computed the total mass concentration of the  
283 aerosol particles suspended in the AIDA chamber. In the first step, the  
284 volume size distribution of the aerosol particles was computed from the com-  
285 bination of the SMPS and APS size spectra, employing a particle density

286 of  $1.72 \text{ g cm}^{-3}$  and a dynamic shape factor of 1.1 to convert the mobility  
287 and aerodynamic diameters from the SMPS and APS measurements into the  
288 equal-volume sphere diameter (Supplementary Fig. 3). The integrated vol-  
289 ume concentration was then multiplied with the particle density to yield the  
290 total mass concentration of the crystallized particle ensemble. Finally, the  
291 smaller mass fraction of AS, which does not contribute to the signature of  
292 the  $\nu_2(\text{NO}_3^-)$  absorption band at  $831 \text{ cm}^{-1}$ , was subtracted to yield the mass  
293 concentration of AN only. The uncertainty for the AN mass density, mainly  
294 arising from the uncertainties associated with the employed values for the  
295 particle density and the dynamic shape factor, was estimated to  $\pm 30\%$ .

## 296 **Remote sensors**

297 CRISTA: The Space Shuttle experiment CRISTA (CRyogenic Infrared Spec-  
298 trometers and Telescopes for the Atmosphere) was flown on the Shuttle Pallet  
299 Satellite in November 1994 (STS 66) and August 1997 (STS 85) [54, 55, 56].  
300 The instrument was equipped with three optical telescopes and four spec-  
301 trometers covering spectral ranges from  $140$  to  $2500 \text{ cm}^{-1}$  using 26 detectors.  
302 The spectral resolution was  $\lambda/\Delta\lambda \approx 500$ , with wavelength  $\lambda$ . In the spectral  
303 range around  $800 \text{ cm}^{-1}$ , this corresponds to a resolution of  $\approx 1.5 \text{ cm}^{-1}$ . Dur-  
304 ing CRISTA-2 (STS85) the main measurement mode covered tangent heights  
305 from 11 to 75 km with a vertical sampling step of 2 km and a vertical field of  
306 view width of about 1.5 km. The horizontal sampling pattern of this mode  
307 was 200 km along track and 650 km across track.

308 MIPAS: The limb-sounder MIPAS (Michelson Interferometer for Passive

309 Atmospheric Sounding) was in operation between 2002 and 2012 on board  
310 the polar orbiting satellite Envisat [57]. It recorded atmospheric emission  
311 spectra in the thermal infrared region between 685 and 2410  $\text{cm}^{-1}$  with spec-  
312 tral resolutions of 0.025  $\text{cm}^{-1}$  in the first measurement period from July 2002  
313 to March 2004 and 0.0625  $\text{cm}^{-1}$  during the second period from January 2005  
314 to April 2012. In nominal rearward viewing limb-scan mode, tangent al-  
315 titudes covered regions between 7 and 72 km with a vertical sampling of  
316 3 km up to 42 km in the period 2002–2004 and 1.5 km up to 22 km altitude  
317 during 2005–2012, respectively. The along-track sampling distance between  
318 limb-scans was 550 km during the first and 420 km during the second mea-  
319 surement period. Retrievals are performed on basis of level-1B calibrated  
320 radiances version 5.02/5.06 provided by ESA.

321 GLORIA: The airborne limb-imaging spectrometer GLORIA (Gimballed  
322 Limb Observer for Radiance Imaging of the Atmosphere) covers the mid-  
323 infrared spectral range from 780 to 1400  $\text{cm}^{-1}$  [35, 36]. During the StratoClim  
324 monsoon campaign, GLORIA was deployed on the Geophysica high-altitude  
325 aircraft performing limb observations with an azimuth of 90° to the right  
326 hand side. Geophysica is a Russian high-altitude aircraft of the type M55,  
327 built and operated by Myasishchev Design Bureau, Zhukovsky, Moscow Re-  
328 gion. GLORIA takes one limb-image of 128 vertical  $\times$  48 horizontal pixels  
329 with a spectral resolution of 0.0625  $\text{cm}^{-1}$  within 13 s. The vertical elevation  
330 coverage is 4.1°. The spectra of horizontal pixel rows are averaged for noise  
331 reduction. In combination with the typical velocity of the aircraft of 700  
332 to 750  $\text{km h}^{-1}$  this corresponds to an along track sampling of around 3 km.  
333 The generation of calibrated spectra from GLORIA observations has been



334 described in [58].

## 335 **Identification and retrieval of ammonium nitrate (AN)** 336 **from infrared limb observations**

337 In previous infrared limb observations, the infrared  $\nu_2$  out-of-plane deforma-  
338 tion band of  $\text{NO}_3^-$  in nitric acid trihydrate (NAT) at  $821\text{ cm}^{-1}$  [59, 60, 61] has  
339 been used to detect and quantify NAT particles within polar stratospheric  
340 clouds [62, 63, 64]. This spectral band is especially suited for detection from  
341 limb-viewing sensors since it is located in one of the window regions in the  
342 mid-infrared least affected by trace gas signatures. Further, compared to  
343 other spectral bands of solids, the nitrate  $\nu_2$  band is so sharp that it can  
344 easily be identified.

345 The  $\nu_2(\text{NO}_3^-)$  - band of ammonium nitrate (AN) has frequently been  
346 assigned in laboratory spectra to wavenumbers around  $831\text{ cm}^{-1}$ :  $830\text{ cm}^{-1}$   
347 [65],  $831\text{--}833\text{ cm}^{-1}$  [66],  $830\text{--}832\text{ cm}^{-1}$  [60],  $831\text{ cm}^{-1}$ [33]. The only field ob-  
348 servations where the  $\nu_2(\text{NO}_3^-)$  band was identified in collected samples of  
349 ambient aerosols have been reported in [67] and, tentatively, in [68].

350 Supplementary Figures 1 and 4 show the detection of the  $\nu_2(\text{NO}_3^-)$  -  
351 band of AN in infrared spectra of the spaceborne limb sounding instruments  
352 CRISTA and MIPAS, as well as observed by GLORIA during the StratoClim  
353 aircraft campaign. From difference spectra of observations at similar tangent  
354 altitudes but at different locations, a spectral band with maximum close to  
355  $831\text{ cm}^{-1}$  and width of about  $3\text{ cm}^{-1}$  could clearly be identified - exactly at the  
356 position of the  $\nu_2(\text{NO}_3^-)$  band of AN. An intensive search for an alternative

357 explanation of this signature, either by other kinds of aerosol particles or by  
358 gas phase species was not successful. For example, AS, ammonium bisulfate  
359  $(\text{NH}_4)\text{HSO}_4$  and letovicite  $(\text{NH}_4)_3\text{H}(\text{SO}_4)_2$  do not show any band around  
360  $830\text{ cm}^{-1}$  [69, 70], as well as mineral dust [71] and dicarboxylic acids like  
361 oxalic acid  $(\text{C}_2\text{H}_2\text{O}_4)$ , malonic acid  $(\text{C}_3\text{H}_4\text{O}_4)$  [72] or succinic acid  $(\text{C}_4\text{H}_6\text{O}_4)$   
362 [73]. Apart from NAT and AN, other nitrates, do show the sharp peak of the  
363  $\nu_2(\text{NO}_3^-)$ -band in the  $820\text{-}840\text{ cm}^{-1}$  region of the infrared spectrum, however,  
364 not at the position of AN, e.g. sodium nitrate  $(\text{NaNO}_3)$  at  $836\text{ cm}^{-1}$  [74, 75],  
365 or potassium nitrate  $(\text{KNO}_3)$  at  $825\text{ cm}^{-1}$  [74].

366 As shown in our AIDA measurements as well as in [33], an aqueous solu-  
367 tion of AN also has a spectral signature in that spectral region (Supplemen-  
368 tary Fig. 3). However, it is clearly distinct from the solid AN peak since its  
369 maximum is located at  $829\text{ cm}^{-1}$  and its width is about twice the width of  
370 the solid AN signature. Thus, it does not fit to our observed spectra (Supple-  
371 mentary Figs. 1 and 4). We, therefore, conclude that the spectral signature  
372 consistently observed inside the AMA by the three different instruments is  
373 caused by aerosol composed of AN in solid state.

374 The absorption coefficients as derived from the aerosol chamber experi-  
375 ments have been used for the retrieval of vertical profiles of AN mass density  
376 from observations of CRISTA, MIPAS and GLORIA. In case of MIPAS and  
377 GLORIA the same processing scheme as used for  $\text{NH}_3$  (see below) has been  
378 applied. For analysis of CRISTA observations, the retrieval employs the pro-  
379 cessing scheme of the airborne successor instrument already used for deriving  
380 PAN in the AMA [76, 19]; the measurement density was improved by synop-  
381 tically interpolating the measurements of five measurement days to a single

382 point of time in the middle by using trajectory calculations. The spectral  
383 window between  $828\text{ cm}^{-1}$  and  $835\text{ cm}^{-1}$  has been commonly evaluated. Un-  
384 certainties for AN mass concentrations are estimated to  $\pm 0.03\text{ }\mu\text{g m}^{-3}$  (single  
385 profile precision)  $\pm 10\%$  (systematic instrumental/retrieval)  $\pm 30\%$  (spectro-  
386 scopic AN absorption coefficients from the AIDA observations) for GLORIA,  
387  $\pm 15\%$  (single profile precision)  $\pm 15\%$  (systematic instrumental/retrieval)  
388  $\pm 30\%$  (spectroscopy AN) for CRISTA, and,  $\pm 0.015\text{ }\mu\text{g m}^{-3}$  (single profile pre-  
389 cision)  $\pm 30\% \pm 0.01\text{ }\mu\text{g m}^{-3}$  (systematic instrumental/retrieval)  $\pm 30\%$  (spec-  
390 troscopy AN) in case of MIPAS. The values of vertical resolutions are 0.8 km  
391 for GLORIA, 2.2 km for CRISTA, and 4.5 km/3.5 km for the retrieval from  
392 the MIPAS observational period 1 and 2, respectively.

### 393 **Identification and retrieval of ammonia ( $\text{NH}_3$ ) from in-** 394 **frared limb observations**

395 Passive remote sounding is especially suited for detection of  $\text{NH}_3$  since it  
396 avoids problems connected to wall-effects [77, 78]. Retrievals of ammonia  
397 vertical volume mixing ratio profiles from MIPAS mean radiance spectra  
398 which were averaged over three months and  $10^\circ$  latitude  $\times$   $10^\circ$  longitude have  
399 been published in [14]. In order to obtain better resolution in time and space,  
400 here we have performed retrievals of  $\text{NH}_3$  from single MIPAS limb-scans. The  
401 profile retrievals have been performed as described in [14]. The inversion  
402 scheme is a nonlinear least squares fitting in a global-fit approach on 1 km  
403 spaced altitude levels [79] regularized by a first-order smoothing operator [80].  
404 The selected spectral windows with  $\text{NH}_3$  signatures are  $965.1\text{--}965.6\text{ cm}^{-1}$

405 and 966.6–967.5  $\text{cm}^{-1}$  for the first MIPAS period 965.125–965.625  $\text{cm}^{-1}$ , and  
406 966.625–967.5  $\text{cm}^{-1}$  for the second period. Resulting profiles of  $\text{NH}_3$  volume  
407 mixing ratio are characterized by a vertical resolution of 4–4.5 km/3.5–4 km  
408 (1st/2nd period). Uncertainties are estimated according to [14] to  $\pm 5$  pptv  
409 (single profile precision) and  $\pm 15\%$  (accuracy).

410 As in the case of MIPAS, inversion of vertical profiles of  $\text{NH}_3$  volume  
411 mixing ratios from GLORIA calibrated limb-radiances has been performed by  
412 application of a constrained nonlinear least-squares fitting scheme, whereby  
413 measurements from all infrared spectra of one GLORIA image are used [81,  
414 82]. The retrievals employ an altitude grid spacing of 0.25 km. For the  
415 spectral fit, the same spectral windows and inversion procedure as in the  
416 case of the MIPAS second measurement period have been used (see above).  
417 Supplementary Fig. 8 shows the spectral evidence for  $\text{NH}_3$  from GLORIA  
418 observations taken at a tangent altitude of 13.7 km during the flight on 31  
419 July 2017 at 4:14 UTC where the retrieval resulted in a value of 920 pptv at  
420 the 13.75 km altitude level. Here the spectral emission lines of  $\text{NH}_3$  are clearly  
421 identified by comparing the simulations including  $\text{NH}_3$  to the simulations  
422 without consideration of  $\text{NH}_3$ . This proves unambiguously the presence of  
423  $\text{NH}_3$  with concentrations near 1 ppbv in the UT. The vertical resolution of  
424 retrieved profiles is about 0.8 km. The vmr profile uncertainties are estimated  
425 based on various parameter uncertainties as described in [81, 82]. They  
426 amount to  $\pm 8$  pptv (single profile precision)  $\pm 20\%$  (accuracy).

## 427 **In situ sensors on board the Geophysica**

428 ERICA (ERc Instrument for the chemical Composition of Aerosols): The  
429 mass spectrometer ERICA is a newly developed in situ instrument com-  
430 bining a laser ablation aerosol mass spectrometer (ERICA-LAMS) similar  
431 to [83, 84] with a flash vaporization/electron impact ionization mass spec-  
432 trometer (ERICA-AMS) based on the Aerodyne Aerosol Mass Spectrometer  
433 (AMS) principle [39]. For a quantitative comparison of the aerosol chemical  
434 composition, mostly data from the AMS component of ERICA was consid-  
435 ered in this study. Here small ensembles of the sampled aerosol particles  
436 with size diameters between 60 nm and approximately  $2\ \mu\text{m}$  are vaporized at  
437  $600^\circ\text{C}$  followed by electron impact ionization of the vapour [39]. The pos-  
438 itive ions are detected by a Time-Of-Flight Mass Spectrometer (TOFMS)  
439 from which the particle chemical composition can be inferred [40]. While the  
440 reproducibility in the laboratory is better than 5% from calibration to cali-  
441 bration, the uncertainty for the aircraft deployment is estimated to  $\pm 30\%$ .  
442 Single particle aerosol composition was determined by the LAMS compo-  
443 nent of ERICA covering a size range from 150 nm to  $2\ \mu\text{m}$ . For each ablated  
444 and analysed aerosol particle, the positive and negative ion mass spectra are  
445 concurrently recorded by two TOFMSs. This way it is possible to unambigu-  
446 ously identify individual particles which contain both sulfate and nitrate, as  
447 can be seen from the example mass spectra in Supplementary Fig. 9. The  
448 ERICA-LAMS and ERICA-AMS instrument combination itself and the cor-  
449 responding sampling inlet system were custom designed similar to [41] for  
450 operation on the high altitude research aircraft Geophysica.

451 UHSAS/COPAS: The ambient aerosol volume density was obtained from  
452 particle size distribution measurements by means of an in-house modified UH-  
453 SAS optical particle counter [37] (mounted underneath the aircraft's wing)  
454 and the high-altitude COPAS condensation particle counter [38]. The UH-  
455 SAS covers a particle size diameter range from 65 nm to 1  $\mu$ m and has been  
456 modified for operation under stratospheric conditions. One more size bin  
457 extending from 10 nm to 65 nm was derived as composite from the COPAS  
458 and the UHSAS data.

459 MAS: The Multiwavelength Aerosol Scatterometer obtained in situ mea-  
460 surements of the aerosol backscatter ratio at 532 nm [85].

## 461 **Trajectory calculations**

462 Two different models for estimation of convective events along backward  
463 trajectories starting at the GLORIA measurement locations have been used,  
464 TRACZILLA and ATLAS.

465 The TRACZILLA diffusive back-trajectories [86] have been calculated  
466 based on ERA5 reanalysis data ( $0.25^\circ \times 0.25^\circ$  horizontal resolution, 137 ver-  
467 tical levels, hourly temporal resolution) using kinematic vertical winds. Clus-  
468 ters of 1000 parcels are released along each tangent point with a time resolu-  
469 tion of 1 hour. The probability of convective influence along the trajectories is  
470 estimated from the high-frequency MSG1 and Himawari geostationary satel-  
471 lites observations of Brightness Temperature (BT). Both satellite images are  
472 used, jointed at  $90^\circ$ E longitude, to cover the whole AMA region extent. The  
473 trajectory is assumed to encounter a convective event when advected below

474 a deep convective cloud, the top pressure of which is estimated from the BT,  
475 following the same approach as presented in [87].

476 Trajectories from the ATLAS model [88] are driven by ECMWF ERA  
477 Interim reanalysis data ( $0.75^\circ \times 0.75^\circ$  horizontal resolution, 6 h temporal res-  
478 olution) and use a log-pressure coordinate (kinematic trajectories). The tra-  
479 jectory model includes a detailed stochastic parameterization of convective  
480 transport driven by ERA Interim convective mass fluxes and detrainment  
481 rates. At every measurement location of GLORIA, 1000 backward ensem-  
482 ble trajectories are started, which take different paths due to the stochastic  
483 nature of the convective transport scheme.

484 Supplementary Figs. 10 and 11 show backward trajectories starting at the  
485 GLORIA measurement locations on 31 Jul 2017 calculated by TRACZILLA  
486 and ATLAS, respectively. For the SW-bound flight leg, exemplary 30 day  
487 non-convective backward trajectories are shown, starting at locations with an  
488  $\text{NH}_3$  concentrations enhancement larger than 0.4 ppbv. For the NE-bound  
489 leg, exemplary trajectories starting in the same altitude range (12–14 km)  
490 are shown for comparison. The trajectories show that the history of the  
491 airmasses corresponding to enhanced  $\text{NH}_3$  concentrations is different from the  
492 one where no  $\text{NH}_3$  has been detected. Further, consistently in both models,  
493 maxima in the convective event density along the trajectories with enhanced  
494  $\text{NH}_3$ , as indicated by white contour lines, are located over the Himalayas  
495 and the Tibetan plateau as well as over NW-India and NE-Pakistan. The  
496 latter region is clearly correlated with a region of high column amounts as  
497 observed by the IASI satellite instruments during the days before the aircraft  
498 observations. Thus, we conclude that it is very likely that the high  $\text{NH}_3$

499 concentrations observed by GLORIA have been injected into the UT over  
500 NW-India and NE-Pakistan by strong convection in a region where, near the  
501 ground, high  $\text{NH}_3$  concentrations are prevalent.



## 502 References

- 503 [1] Dentener, F. J. & Crutzen, P. J. A three-dimensional model of the  
504 global ammonia cycle. *J. Atmos. Chem.* **19**, 331–369 (1994). URL  
505 <https://doi.org/10.1007/BF00694492>.
- 506 [2] Behera, S. N., Sharma, M., Aneja, V. P. & Balasubramanian, R.  
507 Ammonia in the atmosphere: a review on emission sources, atmo-  
508 spheric chemistry and deposition on terrestrial bodies. *Environ. Sci.*  
509 *Pollut. Res.* **20**, 8092–8131 (2013). URL [https://doi.org/10.1007/  
510 s11356-013-2051-9](https://doi.org/10.1007/s11356-013-2051-9).
- 511 [3] Bouwman, A. *et al.* A global high-resolution emission inventory for  
512 ammonia. *Glob. Biogeochem. Cycles* **11**, 561–587 (1997). URL [https:  
513 //doi.org/10.1029/97GB02266](https://doi.org/10.1029/97GB02266).
- 514 [4] Erisman, J. W., Sutton, M. A., Galloway, J., Klimont, Z. & Winiwarter,  
515 W. How a century of ammonia synthesis changed the world. *Nature*  
516 *Geosci.* **1**, 636–639 (2008). URL <https://doi.org/10.1038/ngeo325>.
- 517 [5] Warner, J. X. *et al.* Increased atmospheric ammonia over the world’s  
518 major agricultural areas detected from space. *Geophys. Res. Lett.* **44**,  
519 2875–2884 (2017). URL <https://doi.org/10.1002/2016GL072305>.
- 520 [6] Xu, R. T. *et al.* Half-century ammonia emissions from agricultural  
521 systems in southern Asia: Magnitude, spatiotemporal patterns, and  
522 implications for human health. *Geohealth* **2**, 40–53 (2018). URL  
523 <https://doi.org/10.1002/2017GH000098>.

- 524 [7] Hauglustaine, D. A., Balkanski, Y. & Schulz, M. A global model sim-  
525 ulation of present and future nitrate aerosols and their direct radiative  
526 forcing of climate. *Atmos. Chem. Phys.* **14**, 11031–11063 (2014). URL  
527 <https://doi.org/10.5194/acp-14-11031-2014>.
- 528 [8] IPCC. *Climate Change 2013: The Physical Science Basis. Contribu-*  
529 *tion of Working Group I to the Fifth Assessment Report of the Inter-*  
530 *governmental Panel on Climate Change* (Cambridge University Press,  
531 Cambridge, United Kingdom and New York, NY, USA, 2013). URL  
532 [www.climatechange2013.org](http://www.climatechange2013.org).
- 533 [9] Kirkby, J. *et al.* Role of sulphuric acid, ammonia and galactic cosmic  
534 rays in atmospheric aerosol nucleation. *Nature* **476**, 429–433 (2011).  
535 URL <https://doi.org/10.1038/nature10343>.
- 536 [10] Kürten, A. *et al.* Experimental particle formation rates spanning tro-  
537 pospheric sulfuric acid and ammonia abundances, ion production rates,  
538 and temperatures. *J. Geophys. Res.* **121**, 12,377–12,400 (2016). URL  
539 <https://doi.org/10.1002/2015JD023908>.
- 540 [11] Abbatt, J. P. D. *et al.* Solid ammonium sulfate aerosols as ice nuclei:  
541 A pathway for cirrus cloud formation. *Science* (2006). URL <https://doi.org/10.1126/science.1129726>.
- 543 [12] Cziczo, D. J. & Abbatt, J. P. D. Infrared observations of the response  
544 of NaCl, MgCl<sub>2</sub>, NH<sub>4</sub>HSO<sub>4</sub>, and NH<sub>4</sub>NO<sub>3</sub> aerosols to changes in relative  
545 humidity from 298 to 238 K. *J. Phys. Chem. A* **104**, 2038–2047 (2000).  
546 URL <https://doi.org/10.1021/jp9931408>.

- 547 [13] Cziczo, D. J. & Abbatt, J. P. D. Ice nucleation in  $\text{NH}_4\text{HSO}_4$ ,  $\text{NH}_4\text{NO}_3$ ,  
548 and  $\text{H}_2\text{SO}_4$  aqueous particles: Implications for cirrus cloud formation.  
549 *Geophys. Res. Lett.* **28**, 963–966 (2001). URL [https://doi.org/10.](https://doi.org/10.1029/2000GL012568)  
550 [1029/2000GL012568](https://doi.org/10.1029/2000GL012568).
- 551 [14] Höpfner, M. *et al.* First detection of ammonia ( $\text{NH}_3$ ) in the Asian sum-  
552 mer monsoon upper troposphere. *Atmos. Chem. Phys.* **16**, 14357–14369  
553 (2016). URL <https://doi.org/10.5194/acp-16-14357-2016>.
- 554 [15] Ploeger, F. *et al.* A potential vorticity-based determination of the  
555 transport barrier in the Asian summer monsoon anticyclone. *Atmos.*  
556 *Chem. Phys.* **15**, 13145–13159 (2015). URL [https://doi.org/10.](https://doi.org/10.5194/acp-15-13145-2015)  
557 [5194/acp-15-13145-2015](https://doi.org/10.5194/acp-15-13145-2015).
- 558 [16] Park, M., Randel, W. J., Gettelman, A., Massie, S. T. & Jiang, J. H.  
559 Transport above the Asian summer monsoon anticyclone inferred from  
560 Aura Microwave Limb Sounder tracers. *J. Geophys. Res.* **112**, 253  
561 (2007). URL <https://doi.org/10.1029/2006JD008294>.
- 562 [17] Park, M. *et al.* Chemical isolation in the Asian monsoon anticyclone  
563 observed in Atmospheric Chemistry Experiment (ACE-FTS) data. *At-*  
564 *mos. Chem. Phys.* **8**, 757–764 (2008). URL [https://doi.org/10.5194/](https://doi.org/10.5194/acp-8-757-2008)  
565 [acp-8-757-2008](https://doi.org/10.5194/acp-8-757-2008).
- 566 [18] Randel, W. J. *et al.* Asian monsoon transport of pollution to the strato-  
567 sphere. *Science* **328**, 611–613 (2010). URL [https://doi.org/10.1126/](https://doi.org/10.1126/science.1182274)  
568 [science.1182274](https://doi.org/10.1126/science.1182274).

- 569 [19] Ungermann, J. *et al.* Observations of PAN and its confinement in the  
570 Asian summer monsoon anticyclone in high spatial resolution. *Atmos.*  
571 *Chem. Phys.* **16**, 8389–8403 (2016). URL [https://doi.org/10.5194/  
572 acp-16-8389-2016](https://doi.org/10.5194/acp-16-8389-2016).
- 573 [20] Santee, M. L. *et al.* A comprehensive overview of the climatological  
574 composition of the Asian summer monsoon anticyclone based on 10 years  
575 of Aura Microwave Limb Sounder measurements. *J. Geophys. Res.* **122**,  
576 5491–5514 (2017). URL <https://doi.org/10.1002/2016JD026408>.
- 577 [21] Lelieveld, J. *et al.* The South Asian monsoon: Pollution pump and  
578 purifier. *Science* (2018). URL [https://doi.org/10.1126/science.  
579 aar2501](https://doi.org/10.1126/science.aar2501).
- 580 [22] Ploeger, F., Konopka, P., Walker, K. & Riese, M. Quantifying pol-  
581 lution transport from the Asian monsoon anticyclone into the lower  
582 stratosphere. *Atmos. Chem. Phys.* **17**, 7055–7066 (2017). URL <https://doi.org/10.5194/acp-17-7055-2017>.
- 584 [23] Yu, P. *et al.* Efficient transport of tropospheric aerosol into the strato-  
585 sphere via the Asian summer monsoon anticyclone. *Proc. Natl. Acad.*  
586 *Sci. U.S.A.* **114**, 6972–6977 (2017). URL [https://doi.org/10.1073/  
587 pnas.1701170114](https://doi.org/10.1073/pnas.1701170114).
- 588 [24] Vernier, J.-P., Thomason, L. W. & Kar, J. CALIPSO detection of an  
589 Asian tropopause aerosol layer. *Geophys. Res. Lett.* **38** (2011). URL  
590 <https://doi.org/10.1029/2010GL046614>.

- 591 [25] Thomason, L. W. & Vernier, J.-P. Improved SAGE II cloud/aerosol  
592 categorization and observations of the Asian tropopause aerosol layer:  
593 1989-2005. *Atmos. Chem. Phys.* **13**, 4605–4616 (2013). URL <https://doi.org/10.5194/acp-13-4605-2013>.  
594
- 595 [26] Vernier, J. P. *et al.* Increase in upper tropospheric and lower strato-  
596 spheric aerosol levels and its potential connection with Asian pollution.  
597 *J. Geophys. Res.* **120**, 1608–1619 (2015). URL [https://doi.org/10.](https://doi.org/10.1002/2014JD022372)  
598 [1002/2014JD022372](https://doi.org/10.1002/2014JD022372).
- 599 [27] Vernier, J.-P. *et al.* BATAL: The balloon measurement campaigns of  
600 the Asian tropopause aerosol layer. *Bull. Amer. Met. Soc.* **99**, 955–973  
601 (2018). URL <https://doi.org/10.1175/BAMS-D-17-0014.1>.
- 602 [28] Fadnavis, S. *et al.* Transport of aerosols into the UTLS and their  
603 impact on the Asian monsoon region as seen in a global model sim-  
604 ulation. *Atmos. Chem. Phys.* **13**, 8771–8786 (2013). URL <https://doi.org/10.5194/acp-13-8771-2013>.  
605
- 606 [29] Neely, R. R. *et al.* The contribution of anthropogenic SO<sub>2</sub> emissions to  
607 the Asian tropopause aerosol layer. *J. Geophys. Res.* **119**, 1571–1579  
608 (2014). URL <https://doi.org/10.1002/2013JD020578>.
- 609 [30] Yu, P., Toon, O. B., Neely, R. R., Martinsson, B. G. & Brenninkmeijer,  
610 C. A. M. Composition and physical properties of the Asian tropopause  
611 aerosol layer and the North American tropospheric aerosol layer. *Geo-*  
612 *phys. Res. Lett.* **42**, 2540–2546 (2015). URL [https://doi.org/10.](https://doi.org/10.1002/2015GL063181)  
613 [1002/2015GL063181](https://doi.org/10.1002/2015GL063181).

- 614 [31] Lau, W. K. M., Yuan, C. & Li, Z. Origin, maintenance and variability  
615 of the Asian Tropopause Aerosol Layer (ATAL): The roles of monsoon  
616 dynamics. *Sci. Rep.* **8**, 3960 (2018). URL [https://doi.org/10.1038/  
617 s41598-018-22267-z](https://doi.org/10.1038/s41598-018-22267-z).
- 618 [32] Gu, Y., Liao, H. & Bian, J. Summertime nitrate aerosol in the upper tro-  
619 posphere and lower stratosphere over the Tibetan Plateau and the South  
620 Asian summer monsoon region. *Atmos. Chem. Phys.* **16**, 6641–6663  
621 (2016). URL <https://www.atmos-chem-phys.net/16/6641/2016/>.
- 622 [33] Schlenker, J. C. & Martin, S. T. Crystallization pathways of sulfate-  
623 nitrate-ammonium aerosol particles. *J. Phys. Chem. A* **109**, 9980–9985  
624 (2005). URL <https://doi.org/10.1021/jp052973x>.
- 625 [34] Vogel, B. *et al.* Lagrangian simulations of the transport of young air  
626 masses to the top of the Asian monsoon anticyclone and into the tropical  
627 pipe. *Atmos. Chem. Phys. Discuss.* **2018**, 1–38 (2018). URL [https:  
628 //doi.org/10.5194/acp-2018-724](https://doi.org/10.5194/acp-2018-724).
- 629 [35] Friedl-Vallon, F. *et al.* Instrument concept of the imaging Fourier trans-  
630 form spectrometer GLORIA. *Atmos. Meas. Tech.* **7**, 3565–3577 (2014).  
631 URL <https://doi.org/10.5194/amt-7-3565-2014>.
- 632 [36] Riese, M. *et al.* Gimballed Limb Observer for Radiance Imag-  
633 ing of the Atmosphere (GLORIA) scientific objectives. *Atmos.*  
634 *Meas. Tech.* **7**, 1915–1928 (2014). URL [https://doi.org/10.5194/  
635 amt-7-1915-2014](https://doi.org/10.5194/amt-7-1915-2014).

- 636 [37] Cai, Y., Montague, D. C., Mooiweer-Bryan, W. & Deshler, T. Perfor-  
637 mance characteristics of the ultra high sensitivity aerosol spectrometer  
638 for particles between 55 and 800 nm: Laboratory and field studies. *J.*  
639 *Aerosol Sci.* **39**, 759 – 769 (2008). URL [https://doi.org/10.1016/j.](https://doi.org/10.1016/j.jaerosci.2008.04.007)  
640 [jaerosci.2008.04.007](https://doi.org/10.1016/j.jaerosci.2008.04.007).
- 641 [38] Weigel, R. *et al.* In situ observations of new particle formation in  
642 the tropical upper troposphere: the role of clouds and the nucle-  
643 ation mechanism. *Atmos. Chem. Phys.* **11**, 9983–10010 (2011). URL  
644 <https://doi.org/10.5194/acp-11-9983-2011>.
- 645 [39] Drewnick, F. *et al.* A new time-of-flight aerosol mass spectrometer  
646 (TOF-AMS) - instrument description and first field deployment. *Aerosol*  
647 *Sci. Technol.* **39**, 637–658 (2005). URL [https://doi.org/10.1080/](https://doi.org/10.1080/02786820500182040)  
648 [02786820500182040](https://doi.org/10.1080/02786820500182040).
- 649 [40] Allan, J. D. *et al.* A generalised method for the extraction of chemically  
650 resolved mass spectra from aerodyne aerosol mass spectrometer data. *J.*  
651 *Aerosol Sci.* **35**, 909 – 922 (2004). URL [https://doi.org/10.1016/j.](https://doi.org/10.1016/j.jaerosci.2004.02.007)  
652 [jaerosci.2004.02.007](https://doi.org/10.1016/j.jaerosci.2004.02.007).
- 653 [41] Schulz, C. *et al.* Aircraft-based observations of isoprene-epoxydiol-  
654 derived secondary organic aerosol (IEPOX-SOA) in the tropical upper  
655 troposphere over the Amazon region. *Atmos. Chem. Phys.* **18**, 14979–  
656 15001 (2018). URL <https://doi.org/10.5194/acp-18-14979-2018>.
- 657 [42] Van Damme, M. *et al.* Version 2 of the IASI NH<sub>3</sub> neural network  
658 retrieval algorithm: near-real-time and reanalysed datasets. *Atmos.*

- 659 *Meas. Tech.* **10**, 4905–4914 (2017). URL [https://doi.org/10.5194/](https://doi.org/10.5194/amt-10-4905-2017)  
660 [amt-10-4905-2017](https://doi.org/10.5194/amt-10-4905-2017).
- 661 [43] Clarisse, L., Clerbaux, C., Dentener, F., Hurtmans, D. & Coheur, P.-  
662 F. Global ammonia distribution derived from infrared satellite obser-  
663 vations. *Nature Geosci.* **2**, 479–483 (2009). URL [http://dx.doi.org/](http://dx.doi.org/10.1038/ngeo551)  
664 [10.1038/ngeo551](http://dx.doi.org/10.1038/ngeo551).
- 665 [44] van Damme, M. *et al.* Industrial and agricultural ammonia point sources  
666 exposed. *Nature* **564**, 99 (2018). URL [https://doi.org/10.1038/](https://doi.org/10.1038/s41586-018-0747-1)  
667 [s41586-018-0747-1](https://doi.org/10.1038/s41586-018-0747-1).
- 668 [45] Metzger, S., Dentener, F., Krol, M., Jeuken, A. & Lelieveld, J.  
669 Gas/aerosol partitioning 2. Global modeling results. *J. Geophys. Res.*  
670 **107**, ACH 17–1–ACH 17–23 (2002). URL [https://doi.org/10.1029/](https://doi.org/10.1029/2001JD001103)  
671 [2001JD001103](https://doi.org/10.1029/2001JD001103).
- 672 [46] Hoog, I., Mitra, S. K., Diehl, K. & Borrmann, S. Laboratory stud-  
673 ies about the interaction of ammonia with ice crystals at temperatures  
674 between 0 and  $-20^{\circ}\text{C}$ . *J. Atmos. Chem.* **57**, 73–84 (2007). URL  
675 <https://doi.org/10.1007/s10874-007-9063-0>.
- 676 [47] Jost, A., Szakáll, M., Diehl, K., Mitra, S. K. & Borrmann, S. Chem-  
677 istry of riming: the retention of organic and inorganic atmospheric  
678 trace constituents. *Atmos. Chem. Phys.* **17**, 9717–9732 (2017). URL  
679 <https://doi.org/10.5194/acp-17-9717-2017>.
- 680 [48] Ge, C., Zhu, C., Francisco, J. S., Zeng, X. C. & Wang, J. A molecular  
681 perspective for global modeling of upper atmospheric  $\text{NH}_3$  from freezing



- 682 clouds. *Proc. Natl. Acad. Sci. U.S.A.* (2018). URL [https://doi.org/](https://doi.org/10.1073/pnas.1719949115)  
683 [10.1073/pnas.1719949115](https://doi.org/10.1073/pnas.1719949115).
- 684 [49] Möhler, O. *et al.* Experimental investigation of homogeneous freez-  
685 ing of sulphuric acid particles in the aerosol chamber AIDA. *Atmos.*  
686 *Chem. Phys.* **3**, 211–223 (2003). URL [https://doi.org/10.5194/](https://doi.org/10.5194/acp-3-211-2003)  
687 [acp-3-211-2003](https://doi.org/10.5194/acp-3-211-2003).
- 688 [50] Fahey, D. W. *et al.* The AquaVIT-1 intercomparison of atmospheric  
689 water vapor measurement techniques. *Atmos. Meas. Tech.* **7**, 3177–3213  
690 (2014). URL <https://doi.org/10.5194/amt-7-3177-2014>.
- 691 [51] Wagner, R., Benz, S., Möhler, O., Saathoff, H. & Schurath, U. Prob-  
692 ing ice clouds by broadband mid-infrared extinction spectroscopy: case  
693 studies from ice nucleation experiments in the AIDA aerosol and cloud  
694 chamber. *Atmos. Chem. Phys.* **6**, 4775–4800 (2006). URL [https://](https://doi.org/10.5194/acp-6-4775-2006)  
695 [doi.org/10.5194/acp-6-4775-2006](https://doi.org/10.5194/acp-6-4775-2006).
- 696 [52] Schnaiter, M. *et al.* Influence of particle size and shape on the backscat-  
697 tering linear depolarisation ratio of small ice crystals - cloud chamber  
698 measurements in the context of contrail and cirrus microphysics. *At-*  
699 *mos. Chem. Phys.* **12**, 10465–10484 (2012). URL [https://doi.org/](https://doi.org/10.5194/acp-12-10465-2012)  
700 [10.5194/acp-12-10465-2012](https://doi.org/10.5194/acp-12-10465-2012).
- 701 [53] Wagner, R. *et al.* A review of optical measurements at the aerosol and  
702 cloud chamber AIDA. *J. Quant. Spectrosc. Radiat. Transfer* **110**, 930 –  
703 949 (2009). URL <https://doi.org/10.1016/j.jqsrt.2009.01.026>.

- 704 Light Scattering: Mie and More Commemorating 100 years of Mie's  
705 1908 publication.
- 706 [54] Offermann, D. *et al.* Cryogenic Infrared Spectrometers and Tele-  
707 scopes for the Atmosphere (CRISTA) experiment and middle atmo-  
708 sphere variability. *J. Geophys. Res.* **104**, 16311–16325 (1999). URL  
709 <https://doi.org/10.1029/1998JD100047>.
- 710 [55] Riese, M. *et al.* Cryogenic Infrared Spectrometers and Telescopes for the  
711 Atmosphere (CRISTA) data processing and atmospheric temperature  
712 and trace gas retrieval. *J. Geophys. Res.* **104**, 16349–16367 (1999).  
713 URL <https://doi.org/10.1029/1998JD100057>.
- 714 [56] Grossmann, K. U. *et al.* The CRISTA-2 mission. *J. Geophys. Res.* **107**,  
715 1–1 (2002). URL <https://doi.org/10.1029/2001JD000667>.
- 716 [57] Fischer, H. *et al.* MIPAS: an instrument for atmospheric and climate  
717 research. *Atmos. Chem. Phys.* **8**, 2151–2188 (2008). URL <https://doi.org/10.5194/acp-8-2151-2008>.
- 718
- 719 [58] Kleinert, A. *et al.* Level 0 to 1 processing of the imaging Fourier trans-  
720 form spectrometer GLORIA: generation of radiometrically and spec-  
721 trally calibrated spectra. *Atmos. Meas. Tech.* **7**, 4167–4184 (2014). URL  
722 <https://doi.org/10.5194/amt-7-4167-2014>.
- 723 [59] Toon, O. B., Tolbert, M. A., Middlebrook, A. M. & Jordan, J. Infrared  
724 optical constants of H<sub>2</sub>O, ice, amorphous nitric acid solutions, and nitric  
725 acid hydrates. *J. Geophys. Res.* **99**, 25631–25654 (1994). URL <https://doi.org/10.1029/94JD02388>.
- 726

- 727 [60] Koch, T. G., Holmes, N. S., Roddis, T. B. & Sodeau, J. R. Low-  
728 temperature reflection/absorption IR study of thin films of nitric acid  
729 hydrates and ammonium nitrate adsorbed on gold foil. *J. Chem. Soc.*  
730 *Faraday Trans.* **92**, 4787 (1996). URL [https://doi.org/10.1039/](https://doi.org/10.1039/FT9969204787)  
731 [FT9969204787](https://doi.org/10.1039/FT9969204787).
- 732 [61] Biermann, U. M. *Gefrier- und FTIR-Experimente zur Nukleation und*  
733 *Lebensdauer stratosphärischer Wolken*. Ph.D. thesis, Universität Biele-  
734 feld (1998). Cuvillier Verlag, ISBN 3-89712-212-X.
- 735 [62] Spang, R. & Remedios, J. J. Observations of a distinctive infra-red  
736 spectral feature in the atmospheric spectra of polar stratospheric clouds  
737 measured by the CRISTA instrument. *Geophys. Res. Lett.* **30** (2003).  
738 URL <https://doi.org/10.1029/2003GL017231>.
- 739 [63] Höpfner, M. *et al.* Spectroscopic evidence for NAT, STS, and ice in MI-  
740 PAS infrared limb emission measurements of polar stratospheric clouds.  
741 *Atmos. Chem. Phys.* **6**, 1201–1219 (2006). URL [https://doi.org/10.](https://doi.org/10.5194/acp-6-1201-2006)  
742 [5194/acp-6-1201-2006](https://doi.org/10.5194/acp-6-1201-2006).
- 743 [64] Woiwode, W. *et al.* Spectroscopic evidence of large aspherical  $\beta$ -  
744 NAT particles involved in denitrification in the December 2011 Arc-  
745 tic stratosphere. *Atmos. Chem. Phys.* **16**, 9505–9532 (2016). URL  
746 <https://doi.org/10.5194/acp-16-9505-2016>.
- 747 [65] Théorêt, A. & Sandorfy, C. Infrared spectra and crystalline phase tran-  
748 sitions of ammonium nitrate. *Can. J. Chem.* **42**, 57–62 (1964). URL  
749 <https://doi.org/10.1139/v64-009>.

- 750 [66] Fernandes, J. R., Ganguly, S. & Rao, C. Infrared spectroscopic study  
751 of the phase transitions in CsNO<sub>3</sub>, RbNO<sub>3</sub> and NH<sub>4</sub>NO<sub>3</sub>. *Spectrochim.*  
752 *Acta A Mol. Biomol. Spectrosc.* **35**, 1013–1020 (1979). URL [https://doi.org/10.1016/0584-8539\(79\)80001-X](https://doi.org/10.1016/0584-8539(79)80001-X).  
753
- 754 [67] Allen, D. T., Palen, E. J., Haimov, M. I., Hering, S. V. & Young,  
755 J. R. Fourier transform infrared spectroscopy of aerosol collected in  
756 a low pressure impactor (LPI/FTIR): Method development and field  
757 calibration. *Aerosol Sci. Technol.* **21**, 325–342 (1994). URL <https://doi.org/10.1080/02786829408959719>.  
758
- 759 [68] Hopey, J. A., Fuller, K. A., Krishnaswamy, V., Bowdle, D. & Newchurch,  
760 M. J. Fourier transform infrared spectroscopy of size-segregated aerosol  
761 deposits on foil substrates. *Appl. Optics* **47**, 2266 (2008). URL <https://doi.org/10.1364/AO.47.002266>.  
762
- 763 [69] Earle, M. E., Pancescu, R. G., Cosic, B., Zsetsky, A. Y. & Sloan,  
764 J. J. Temperature-dependent complex indices of refraction for crystalline  
765 (NH<sub>4</sub>)<sub>2</sub>SO<sub>4</sub>. *J. Phys. Chem. A* **110**, 13022–13028 (2006). URL <https://doi.org/10.1021/jp064704s>.  
766
- 767 [70] Rosenoern, T., Schlenker, J. C. & Martin, S. T. Hygroscopic growth of  
768 multicomponent aerosol particles influenced by several cycles of relative  
769 humidity. *J. Phys. Chem. A* **112**, 2378–2385 (2008). URL <https://doi.org/10.1021/jp0771825>.  
770
- 771 [71] Laskina, O., Young, M. A., Kleiber, P. D. & Grassian, V. H. In-  
772 frared extinction spectra of mineral dust aerosol: Single components

- 773 and complex mixtures. *J. Geophys. Res.* **117** (2012). URL <https://doi.org/10.1029/2012JD017756>.  
774
- 775 [72] Braban, C. F., Carroll, M. F., Styler, S. A. & Abbatt, J. P. D. Phase  
776 transitions of malonic and oxalic acid aerosols. *J. Phys. Chem. A* **107**,  
777 6594–6602 (2003). URL <https://doi.org/10.1021/jp034483f>.
- 778 [73] Miñambres, L., Sánchez, M. N., Castaño, F. & Basterretxea, F. J. Hy-  
779 groscopic properties of internally mixed particles of ammonium sulfate  
780 and succinic acid studied by infrared spectroscopy. *J. Phys. Chem. A*  
781 **114**, 6124–6130 (2010). URL <https://doi.org/10.1021/jp101149k>.
- 782 [74] Chasan, D. E. & Norwitz, G. Infrared determination of inorganic ni-  
783 trates by the pellet technique; infrared determination of two inorganic  
784 nitrates in the presence of each other. *Appl. Spectrosc.* **24**, 283–287  
785 (1970). URL <https://doi.org/10.1366/000370270774371994>.
- 786 [75] Harris, M. J., Salje, E. K. H. & Guttler, B. K. An infrared spectroscopic  
787 study of the internal modes of sodium nitrate: Implications for the  
788 structural phase transition. *J. Phys. Condens. Matter* **2**, 5517–5527  
789 (1990). URL <https://doi.org/10.1088/0953-8984/2/25/004>.
- 790 [76] Ungermann, J. *et al.* CRISTA-NF measurements with unprecedented  
791 vertical resolution during the RECONCILE aircraft campaign. *Atmos.*  
792 *Meas. Tech.* **5**, 1173–1191 (2012). URL [https://doi.org/10.5194/](https://doi.org/10.5194/amt-5-1173-2012)  
793 [amt-5-1173-2012](https://doi.org/10.5194/amt-5-1173-2012).
- 794 [77] Sutton, M. A., Erisman, J. W., Dentener, F. & Möller, D. Ammonia in  
795 the environment: From ancient times to the present. *Environ. Pollut.*

- 796 **156**, 583 – 604 (2008). URL [https://doi.org/10.1016/j.envpol.](https://doi.org/10.1016/j.envpol.2008.03.013)  
797 2008.03.013.
- 798 [78] von Bobruzki, K. *et al.* Field inter-comparison of eleven atmospheric  
799 ammonia measurement techniques. *Atmos. Meas. Tech.* **3**, 91–112  
800 (2010). URL <https://doi.org/10.5194/amt-3-91-2010>.
- 801 [79] von Clarmann, T. *et al.* Retrieval of temperature, H<sub>2</sub>O, O<sub>3</sub>, HNO<sub>3</sub>, CH<sub>4</sub>,  
802 N<sub>2</sub>O, ClONO<sub>2</sub> and ClO from MIPAS reduced resolution nominal mode  
803 limb emission measurements. *Atmos. Meas. Tech.* **2**, 159–175 (2009).  
804 URL <https://doi.org/10.5194/amt-2-159-2009>.
- 805 [80] Tikhonov, A. On the solution of incorrectly stated problems and method  
806 of regularization. *Dokl. Akad. Nauk. SSSR* **151**, 501–504 (1963).
- 807 [81] Woiwode, W. *et al.* Validation of first chemistry mode retrieval results  
808 from the new limb-imaging FTS GLORIA with correlative MIPAS-STR  
809 observations. *Atmos. Meas. Tech.* **8**, 2509–2520 (2015). URL <https://doi.org/10.5194/amt-8-2509-2015>.  
810
- 811 [82] Johansson, S. *et al.* Airborne limb-imaging measurements of tem-  
812 perature, HNO<sub>3</sub>, O<sub>3</sub>, ClONO<sub>2</sub>, H<sub>2</sub>O and CFC-12 during the Arc-  
813 tic winter 2015/16: characterization, in situ validation and compari-  
814 son to Aura/MLS. *Atmos. Meas. Tech.* **11**, 4737–4756 (2018). URL  
815 <https://doi.org/10.5194/amt-11-4737-2018>.
- 816 [83] Brands, M. *et al.* Characterization of a newly developed aircraft-based  
817 laser ablation aerosol mass spectrometer (ALABAMA) and first field

- 818 deployment in urban pollution plumes over Paris during MEGAPOLI  
819 2009. *Aerosol Sci. Technol.* **45**, 46–64 (2011). URL [https://doi.org/](https://doi.org/10.1080/02786826.2010.517813)  
820 [10.1080/02786826.2010.517813](https://doi.org/10.1080/02786826.2010.517813).
- 821 [84] Murphy, D. M. & Thomson, D. S. Laser ionization mass spectroscopy of  
822 single aerosol particles. *Aerosol Sci. Technol.* **22**, 237–249 (1995). URL  
823 <https://doi.org/10.1080/02786829408959743>.
- 824 [85] Cairo, F. *et al.* A comparison of light backscattering and particle size  
825 distribution measurements in tropical cirrus clouds. *Atmos. Meas. Tech.*  
826 **4**, 557–570 (2011). URL <https://doi.org/10.5194/amt-4-557-2011>.
- 827 [86] Pisso, I. & Legras, B. Turbulent vertical diffusivity in the sub-tropical  
828 stratosphere. *Atmos. Chem. Phys.* **8**, 697–707 (2008). URL <https://doi.org/10.5194/acp-8-697-2008>.
- 830 [87] Tissier, A.-S. & Legras, B. Convective sources of trajectories travers-  
831 ing the tropical tropopause layer. *Atmos. Chem. Phys.* **16**, 3383–3398  
832 (2016). URL <https://doi.org/10.5194/acp-16-3383-2016>.
- 833 [88] Wohltmann, I. & Rex, M. The Lagrangian chemistry and trans-  
834 port model ATLAS: validation of advective transport and mixing.  
835 *Geosci. Mod. Dev.* **2**, 153–173 (2009). URL [https://doi.org/10.](https://doi.org/10.5194/gmd-2-153-2009)  
836 [5194/gmd-2-153-2009](https://doi.org/10.5194/gmd-2-153-2009).

## 837 **Acknowledgements**

838 We acknowledge the Geophysica pilots and crew as well as the local support  
839 in Kathmandu. We are grateful to the instrument development and operation  
840 teams of GLORIA at KIT and Jülich, and of ERICA at MPI-C and IPA-  
841 JGU and to the technical team of AIDA at KIT. The work at KIT and Jülich  
842 was supported by the Helmholtz ATMO program. We would like to thank  
843 the teams at ULB/LATMOS (Université Libre de Bruxelles/Laboratoire At-  
844 mosphères, Milieux, Observations Spatiales) for provision of IASI NH<sub>3</sub> data.  
845 The European Space Agency (ESA) is acknowledged for MIPAS data pro-  
846 vision. Meteorological analysis data have been provided by the European  
847 Centre for Medium-Range Weather Forecasts (ECMWF). ERA5 trajecto-  
848 ries computations were generated using Copernicus Climate Change Service  
849 Information. D. Offermann and his team are acknowledged for conducting  
850 CRISTA observations in the AMA region. We thank M.L. Santee for helpful  
851 discussions on satellite datasets. Funding for the ERICA instrument develop-  
852 ment was provided by the European Research Council ERC Advanced Grant  
853 of S.Bo. (EXCATRO project, Grant No. 321040). Part of this work was  
854 supported by the European Community's Seventh Framework Programme  
855 (FP7/2007 - 2013) under grant agreement no. 603557, CEFIPRA5607-1,  
856 ANR-17-CE01-0015. We also thank the Aeris data infrastructure for provid-  
857 ing access to the MSG1 and Himawari data.



## 858 **Author contributions**

859 M.H. conducted the analysis of MIPAS and GLORIA data, produced Figs. 2–  
860 4, and wrote the paper with all authors contributing. J.U. conducted the  
861 analysis of CRISTA data, helped with analysis of GLORIA data and pro-  
862 duced Fig. 1. A.D., S.M., A.B., O.A., A.H., and S.Bo. performed and  
863 analysed the aircraft in situ measurements of ERICA. C.M. and R.We. pre-  
864 pared the analyses for Fig. 4a, O.A. for Fig. 4b. C.M. and R.We. conducted  
865 the measurements and data analyses for UHSAS and COPAS, respectively.  
866 R.W., H.S., O.M., and T.L. conceived and performed the AIDA experiments  
867 and contributed to their interpretation. R.S. discovered the AN emission fea-  
868 ture in CRISTA data for the first time. M.Ri. conceived the reanalysis of the  
869 CRISTA data wrt. signals of the ATAL. G.S. contributed to the analysis of  
870 MIPAS data. B.L. and S.Bu. conducted the TRACZILLA trajectory calcu-  
871 lations. F.C. performed the MAS aircraft observations and conducted their  
872 analysis. F.F.V. conducted the GLORIA aircraft observations. S.J. analysed  
873 the trajectory datasets in combination with the IASI measurements. S.J. and  
874 L.K. helped with analysis of GLORIA data. P.P. contributed to the CRISTA  
875 and GLORIA data analysis. T.N. helped with performing the GLORIA ob-  
876 servations. R.M. contributed to the interpretation of the observations. J.O.  
877 contributed to the interpretation of spectroscopic issues of AN and NH<sub>3</sub>. F.S.  
878 and M.Re. defined the flight region, the general approach, general flight pat-  
879 terns and instrumentation of the aircraft campaign and organized it. I.W.  
880 developed the ATLAS model and provided the trajectory calculations from  
881 it, with contributions from M.Re.

## 882 **Corresponding author**

883 Correspondence and requests for materials should be addressed to M.H.  
884 (michael.hoepfner@kit.edu).

## 885 **Competing interests**

886 The authors declare no competing interests.

## 887 **Data availability**

888 The datasets generated and analysed during the current study are avail-  
889 able from the corresponding author on request. Additionally, the CRISTA  
890 dataset of ammonium nitrate is publicly available at: <https://datapub.fz-juelich.de/slcs/crista/an/>. MIPAS and GLORIA data of ammonia  
891 and ammonium nitrate as well as trajectory information and AIDA spectra  
892 can be downloaded from the KITopen archive at: <https://doi.org/>?. IASI  
893 data on NH<sub>3</sub> are available at <http://iasi.aeris-data.fr/NH3/>.

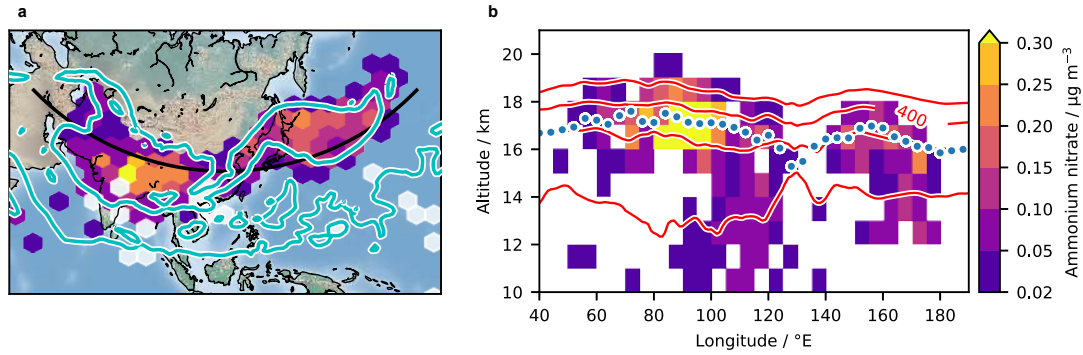


Fig. 1: **Ammonium nitrate observed by CRISTA in the UT 1997.** Cross sections of synoptically interpolated AN mass concentrations, **a**, at 380 K potential temperature (16–17 km altitude), as well as, **b**, at 30°N derived from CRISTA observations between 8 and 16 August 1997. The cyan line in panel **a** shows the 4.1 PVU potential vorticity contour line, a rough measure for the extent of the AMA core, white hexagons indicate missing data and the black line the position of the cross-section of panel **b**. Red lines in panel **b** show potential temperature (K) and blue dots the location of the lapse rate tropopause.

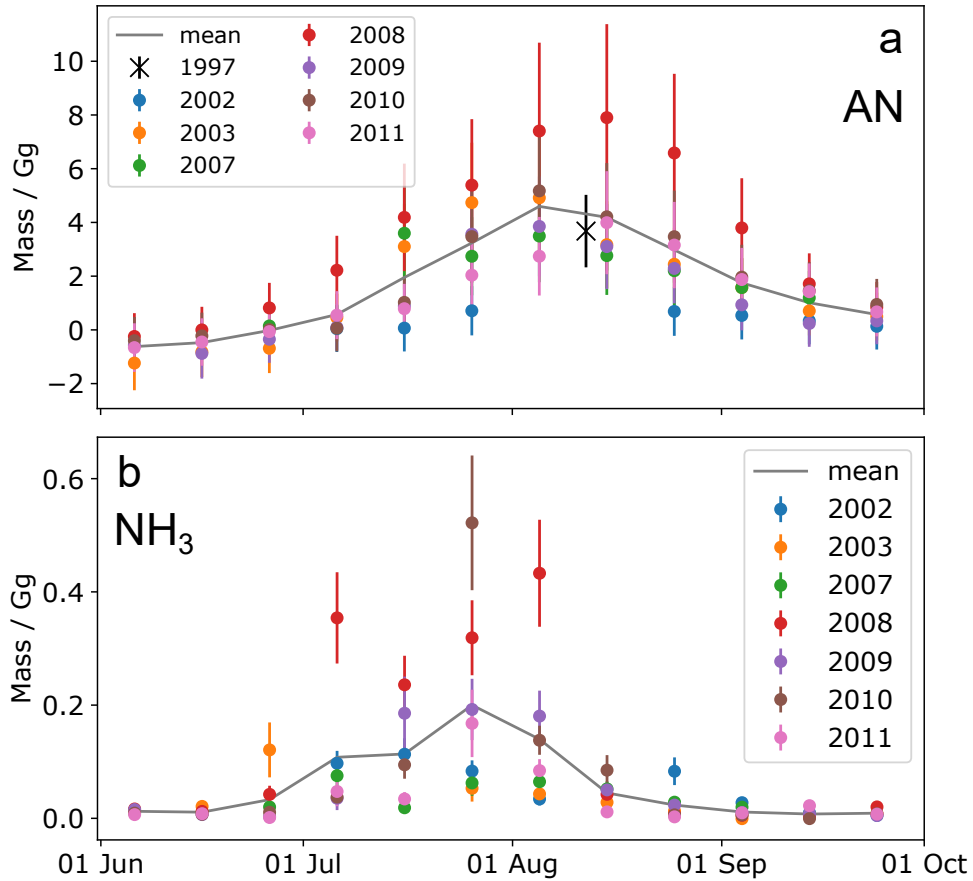


Fig. 2: **Time series of AN and NH<sub>3</sub> in the AMA.** Time series of total mass of **a**, AN, and **b**, NH<sub>3</sub> as derived from MIPAS observations for the region 10°E–110°E, 20°N–40°N and 13–17 km altitude. CRISTA observations of AN are included in **a** as a black cross. Error bars are Gaussian combinations of the estimated retrieval errors (see Methods) and the standard deviations of the mean values.

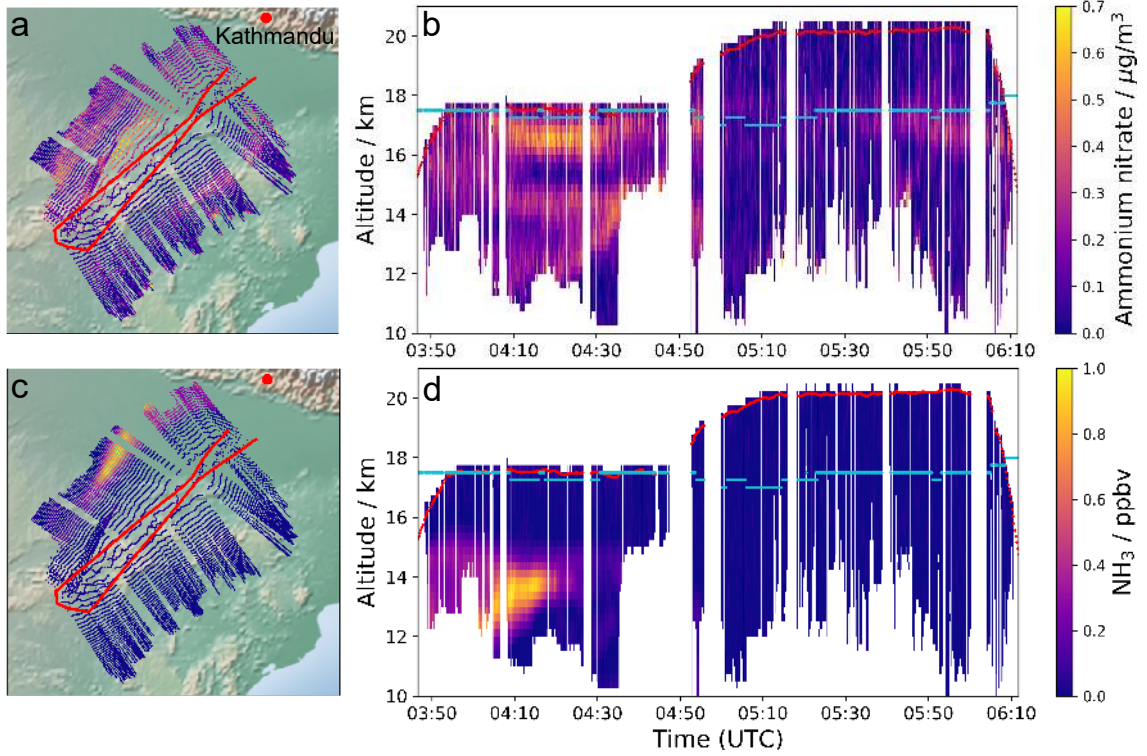


Fig. 3: Airborne limb-imaging observations of AN and  $\text{NH}_3$  in the UT above India during the 2017 Asian monsoon season. **a,b**, altitude-time horizontal projections of AN mass densities, and **c,d**,  $\text{NH}_3$  volume mixing ratios derived from GLORIA measurements during the Geophysica flight on 31 July 2017. Horizontal projection at tangent points (**a,c**) and vertical projection (**b,d**). Vertical resolution and estimated uncertainty (precision, accuracy): AN: 0.8 km,  $\pm 0.03 \mu\text{g m}^{-3} \pm 30\%$ ;  $\text{NH}_3$ : 0.8 km,  $\pm 8 \text{ pptv} \pm 20\%$ ; . Red lines: aircraft position (**a,c**) and altitude (**b,d**), light blue lines (**b,d**): lapse rate tropopause.

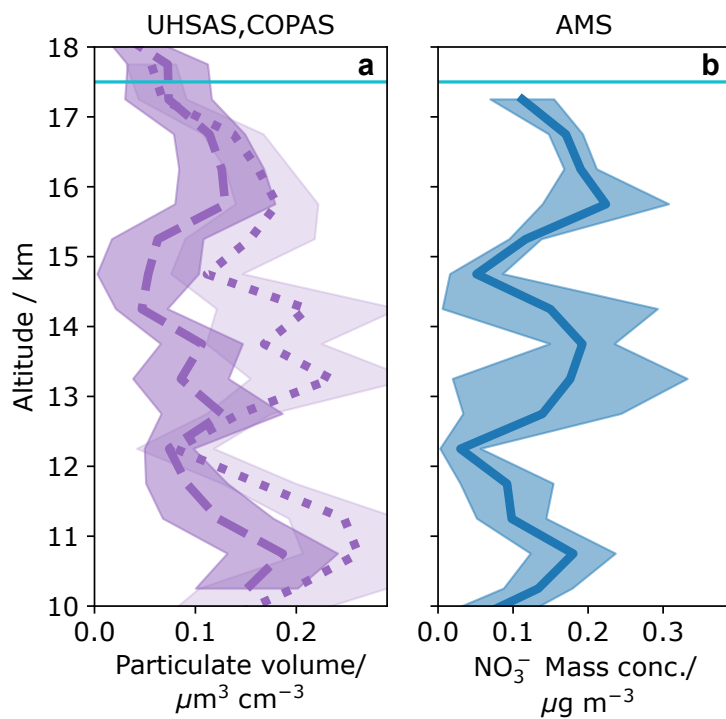


Fig. 4: Airborne in-situ aerosol observations in the Asian monsoon UT on 31 July 2017. a, UHSAS and COPAS derived aerosol volume density during ascent (dashed) and descent (dotted) at Kathmandu. b, ERICA-AMS particulate  $\text{NO}_3^-$  mass concentrations. The values are averages in vertical bins of 0.25 km. For the nitrate content of ERICA-AMS, the uncertainty is estimated to 30%. The estimated uncertainty of the UHSAS and COPAS data is below 30%. Light blue lines indicate the lapse rate tropopause.

# Ammonium nitrate particles formed in upper troposphere sourced from ground ammonia during Asian monsoons

Michael Höpfner<sup>1</sup>, Jörn Ungermann<sup>2</sup>, Stephan Borrmann<sup>3,4</sup>, Robert Wagner<sup>1</sup>, Reinhold Spang<sup>2</sup>, Martin Riese<sup>2,5</sup>, Gabriele Stiller<sup>1</sup>, Oliver Appel<sup>3,4</sup>, Anneke M. Batenburg<sup>3,4</sup>, Silvia Bucci<sup>6</sup>, Francesco Cairo<sup>7</sup>, Antonis Dragoneas<sup>3,4</sup>, Felix Friedl-Vallon<sup>1</sup>, Andreas Hünig<sup>3,4</sup>, Sören Johansson<sup>1</sup>, Lukas Krasaukas<sup>2</sup>, Bernard Legras<sup>6</sup>, Thomas Leisner<sup>1</sup>, Christoph Mahnke<sup>3,4</sup>, Ottmar Möhler<sup>1</sup>, Sergej Molleker<sup>3,4</sup>, Rolf Müller<sup>2</sup>, Tom Neubert<sup>8</sup>, Johannes Orphal<sup>1</sup>, Peter Preusse<sup>2</sup>, Markus Rex<sup>9</sup>, Harald Saathoff<sup>1</sup>, Fred Stroh<sup>2</sup>, Ralf Weigel<sup>4</sup>, and Ingo Wohltmann<sup>9</sup>

<sup>1</sup>Institute of Meteorology and Climate Research, Karlsruhe Institute of Technology, Karlsruhe, Germany

<sup>2</sup>Institute of Energy and Climate Research, Stratosphere, Forschungszentrum Jülich, Jülich, Germany

<sup>3</sup>Department for Particle Chemistry, Max Planck Institute for Chemistry, Mainz, Germany

<sup>4</sup>Institute for Atmospheric Physics, Johannes Gutenberg University, Mainz, Germany

<sup>5</sup>Institute for Atmospheric and Environmental Research, University of Wuppertal, Wuppertal, Germany

<sup>6</sup>Laboratoire de Météorologie Dynamique, UMR8539, IPSL, CNRS/PSL-ENS/Sorbonne Université/École polytechnique, Paris, France

<sup>7</sup>Institute of Atmospheric Sciences and Climate, ISAC-CNR, Rome, Italy

<sup>8</sup>Central Institute of Engineering, Electronics and Analytics - Electronic Systems, Forschungszentrum Jülich, Jülich, Germany

<sup>9</sup>Alfred Wegener Institute, Helmholtz Center for Polar and Marine Research, Potsdam, Germany

## Supplementary discussion of the AIDA cloud chamber observations

Supplementary Figure 1 shows the infrared spectrum of supercooled liquid AN solution droplets in the regime of the  $\nu_2(\text{NO}_3^-)$  absorption band (blue line), which was recorded after nebulization of the 100 mol% AN solution, drying of the aerosol flow to  $\text{RH} \leq 3\%$ , and injection into the AIDA chamber at 61% RH and 223 K. The complete mid-infrared spectrum (shown as trace A in Supplementary Fig. 2, top panel: 6000–800  $\text{cm}^{-1}$ , lower panel: expanded view from 1600 to 800  $\text{cm}^{-1}$ ) proves the liquid phase of the injected aerosol particles by showing the characteristic infrared signature of liquid water centred at about 3500  $\text{cm}^{-1}$  [1, 2]. Furthermore, the recorded depolarization ratio of the aerosol particles at 488 nm and 178° scattering angle (see Methods) was less than 1%, as indicative of spherical, aqueous solution droplets. The strategy of this experiment was similar to the one adopted by [1], namely to confirm the crystallization of AN by exploiting the hysteresis effect in the deliquescence and efflorescence behaviour. According to the Aerosol Inorganics Model (AIM), the deliquescence relative humidity (DRH) of AN at 223 K is 97% [3]. If the AN solution droplets had fully crystallized at  $\leq 3\%$  RH prior to the injection into the AIDA vessel, the particles should not have taken up any liquid water in the chamber, given that the prevalent RH was well below the DRH. The AN particles were kept for an observation period of almost four hours in the AIDA chamber at 223 K and 61% RH, without showing any increase in the depolarization ratio or change in the infrared spectral signature. Our experiment thus corroborates previous studies that have demonstrated the strong inhibition of efflorescence for pure AN solution droplets [4, 5, 1]. The infrared spectrum of liquid AN (Supplementary Fig. 1), however, clearly fails to reproduce the measurement by the CRISTA limb-sounder.

Whereas pure AN solution droplets have a strong tendency to remain in the supercooled liquid state, the crystallization of AN is facilitated by impurities in the aqueous solutions [5], the presence of insoluble inclusions like mineral dust [6], and/or the admixture of compounds that easily crystallize and thereby serve as heterogeneous nuclei to promote the formation of solid AN [1]. Additionally, contact efflorescence initiated by externally located solid particles has been established as a pathway for the crystallization of supersaturated aqueous AN particles [7]. Internal mixtures of ammonium, nitrate, and sulfate are considered as a common



aerosol particle type in the troposphere, and their crystallization behaviour has been thoroughly investigated in aerosol flow tube studies conducted at room temperature [1, 8]. For example, it was shown that the addition of just 10 mol% ammonium sulfate (AS) promoted the crystallization of AN in mixed AN/AS solution droplets [1]. We were able to reproduce this finding in our AIDA experiments. When using a 90 mol% AN + 10 mol% AS bulk solution for aerosol generation, the infrared spectrum of the injected particles (Supplementary Fig. 2, trace C) was devoid of any liquid water signature. Instead, the spectral changes in the band system between 1500 and 1300  $\text{cm}^{-1}$  as well as the appearance of the sharp peak at 831  $\text{cm}^{-1}$  indicated the presence of crystalline AN. In accordance with the prevalence of crystalline particles, the back-scattering linear depolarization ratio adopted a value of 17%. The sulfate admixture was seen by the absorption band at about 1100  $\text{cm}^{-1}$ , which can be due to pure crystalline AS or the double salts 2AN·AS and 3AN·AS [9, 1].

We also investigated whether smaller admixtures of AS were still sufficient to trigger the crystallization of mixed AN/AS solution droplets. As shown by spectrum B in Supplementary Fig. 2, we were able to produce crystalline AN particles even for an AS mole fraction as low as 2.9 mol%. For this mixture, however, the AIDA chamber had to be kept at a lower RH (22%) in order to observe the instantaneous formation of crystalline particles upon aerosol injection. When the AIDA chamber was kept at 61% RH, the injected aerosol particles generated from the 97.1 mol% AN + 2.9 mol% AS bulk solution initially showed the infrared signature representative of supercooled solution droplets with a depolarization ratio  $< 1\%$ . In contrast to the experiment with pure AN solution droplets, the mixed AN/AS particles gradually crystallized while suspended in the AIDA chamber at 223 K and 61% RH for four hours, as evidenced by an increase of the depolarization ratio from  $< 1$  to 5% and a concomitant change of the infrared spectral signature. Spectrum D in Supplementary Fig. 2 illustrates the difference in the spectral signature after the observation time of four hours, demonstrating the formation of the crystalline AN phase. From the infrared spectra, we estimated that about 25% of the aerosol population had crystallized within four hours of observation. Supplementary Figure 1 demonstrates that the  $\nu_2(\text{NO}_3^-)$  band of crystalline AN recorded in the AIDA chamber (orange line, enlarged view of spectrum B from Supplementary Fig. 2) shows a very good match with the CRISTA observation. To the best of our knowledge, the AIDA spectrum represents the first infrared measurement of suspended, crystalline AN particles at temperature conditions of the UT. The crystallization experiments underline that small amounts of sulfate impurities are sufficient to enable the formation of the

solid phase of AN.

Trace E in Supplementary Fig. 2 (bottom) shows the previously recorded infrared spectrum of crystalline AN/AS particles with 10 mol% AS at room temperature [1]. In comparison with the corresponding AIDA spectrum recorded at 223 K (trace C), there are small changes in the fine structure of the band system between 1500 and 1300  $\text{cm}^{-1}$  with contributions from the  $\nu_4(\text{NH}_4^+)$  and  $\nu_3(\text{NO}_3^-)$  modes. These spectral changes could be indicative of a thermal phase transition, given that five different phases of crystalline AN have been reported at ambient pressure [10, 11]. In particular, the phase transition from phase IV to V, which is supposed to occur at 255 K, could account for the temperature-dependent changes in the spectral habitus at 1500 –1300  $\text{cm}^{-1}$ . In contrast to this wavenumber regime, previous infrared studies with thin films of AN have shown that the peak position of the  $\nu_2(\text{NO}_3^-)$  mode is rather insensitive to the transition between phase IV and V [12, 13, 14]. This is corroborated by our findings shown in the left part of Supplementary Fig. 3, where we show the spectral regime of the  $\nu_2$  band of AN particles in the liquid and solid phase recorded during the AIDA experiments at 223 K and the flow-tube studies performed at 293 K by [1]. Obviously, the spectral habitus of the  $\nu_2(\text{NO}_3^-)$  mode does not change with temperature, both for the liquid and the solid phase.

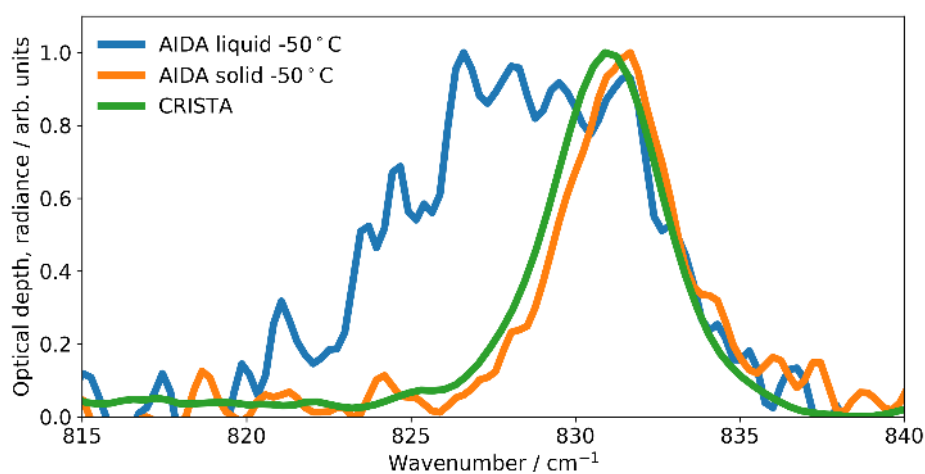
As outlined in the Methods section, the infrared optical depths recorded could be quantitatively scaled by the mass concentration of the suspended aerosol particles, thereby yielding mass specific absorption coefficients of the  $\nu_2(\text{NO}_3^-)$  mode of AN. A representative volume size distribution of the aerosol particles from the crystallization experiment with 97.1 mol% AN + 2.9 mol% AS at 223 K and 22% RH, which was used to derive the aerosol mass concentration, is shown in the right part of Supplementary Fig. 3.

## References

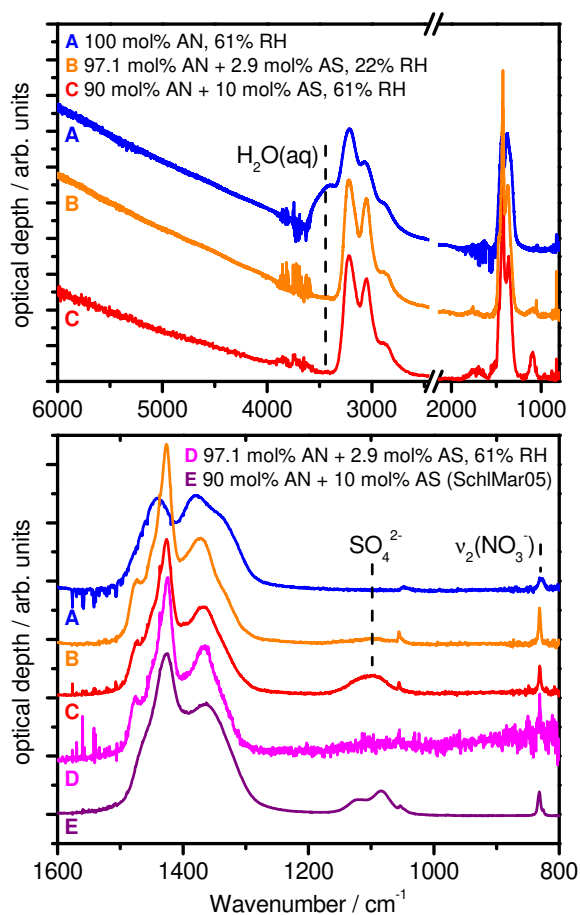
- [1] Schlenker, J. C. & Martin, S. T. Crystallization pathways of sulfate-nitrate-ammonium aerosol particles. *J. Phys. Chem. A* **109**, 9980–9985 (2005). URL <https://doi.org/10.1021/jp052973x>.
- [2] Schuttlefield, J., Al-Hosney, H., Zachariah, A. & Grassian, V. H. Attenuated total reflection fourier transform infrared spectroscopy to investigate water uptake and phase transitions in atmospherically relevant particles. *Appl. Spectrosc.* **61**, 283–292 (2007). URL <https://doi.org/10.1366/000370207780220868>.
- [3] Clegg, S. L., Brimblecombe, P. & Wexler, A. S. Thermodynamic model of the system  $\text{H}^+$ - $\text{NH}_4^+$ - $\text{SO}_4^{2-}$ - $\text{NO}_3^-$ - $\text{H}_2\text{O}$  at tropospheric temperatures. *J. Phys. Chem. A* **102**, 2137–2154 (1998). URL <https://doi.org/10.1021/jp973042r>.
- [4] Cziczo, D. J. & Abbatt, J. P. D. Infrared observations of the response of NaCl, MgCl<sub>2</sub>, NH<sub>4</sub>HSO<sub>4</sub>, and NH<sub>4</sub>NO<sub>3</sub> aerosols to changes in relative humidity from 298 to 238 K. *J. Phys. Chem. A* **104**, 2038–2047 (2000). URL <https://doi.org/10.1021/jp9931408>.
- [5] Lightstone, J. M., Onasch, T. B., Imre, D. & Oatis, S. Deliquescence, efflorescence, and water activity in ammonium nitrate and mixed ammonium nitrate/succinic acid microparticles. *J. Phys. Chem. A* **104**, 9337–9346 (2000). URL <https://doi.org/10.1021/jp002137h>.
- [6] Han, J.-H., Hung, H.-M. & Martin, S. T. Size effect of hematite and corundum inclusions on the efflorescence relative humidities of aqueous ammonium nitrate particles. *J. Geophys. Res.* **107**, AAC 3–1–AAC 3–9 (2002). URL <https://doi.org/10.1029/2001JD001054>.
- [7] Davis, R. D., Lance, S., Gordon, J. A., Ushijima, S. B. & Tolbert, M. A. Contact efflorescence as a pathway for crystallization of atmospherically relevant particles. *Proc. Natl. Acad. Sci. U.S.A.* **112**, 15815–15820 (2015). URL <https://doi.org/10.1073/pnas.1522860113>.
- [8] Schlenker, J. C., Malinowski, A., Martin, S. T., Hung, H.-M. & Rudich, Y. Crystals formed at 293 K by aqueous sulfate-nitrate-ammonium-proton aerosol particles. *J. Phys. Chem. A* **108**, 9375–9383 (2004). URL <https://doi.org/10.1021/jp047836z>.

- [9] Bothe, J. R. & Beyer, K. D. Experimental determination of the  $\text{NH}_4\text{NO}_3/(\text{NH}_4)_2\text{SO}_4/\text{H}_2\text{O}$  phase diagram. *J. Phys. Chem. A* **111**, 12106–12117 (2007). URL <https://doi.org/10.1021/jp0760859>. PMID: 17994714.
- [10] Chellappa, R. S., Dattelbaum, D. M., Velisavljevic, N. & Sheffield, S. The phase diagram of ammonium nitrate. *J. Chem. Phys.* **137**, 064504 (2012). URL <https://doi.org/10.1063/1.4733330>.
- [11] Herrmann, M. J. & Engel, W. Phase transitions and lattice dynamics of ammonium nitrate. *Propellants Explos. Pyrotech.* **22**, 143–147 (1997). URL <https://doi.org/10.1002/prop.19970220308>.
- [12] Fernandes, J. R., Ganguly, S. & Rao, C. Infrared spectroscopic study of the phase transitions in  $\text{CsNO}_3$ ,  $\text{RbNO}_3$  and  $\text{NH}_4\text{NO}_3$ . *Spectrochim. Acta A Mol. Biomol. Spectrosc.* **35**, 1013–1020 (1979). URL [https://doi.org/10.1016/0584-8539\(79\)80001-X](https://doi.org/10.1016/0584-8539(79)80001-X).
- [13] Koch, T. G., Holmes, N. S., Roddis, T. B. & Sodeau, J. R. Low-temperature reflection/absorption IR study of thin films of nitric acid hydrates and ammonium nitrate adsorbed on gold foil. *J. Chem. Soc. Faraday Trans.* **92**, 4787 (1996). URL <https://doi.org/10.1039/FT9969204787>.
- [14] Théorêt, A. & Sandorfy, C. Infrared spectra and crystalline phase transitions of ammonium nitrate. *Can. J. Chem.* **42**, 57–62 (1964). URL <https://doi.org/10.1139/v64-009>.
- [15] Offermann, D. *et al.* Cryogenic Infrared Spectrometers and Telescopes for the Atmosphere (CRISTA) experiment and middle atmosphere variability. *J. Geophys. Res.* **104**, 16311–16325 (1999). URL <https://doi.org/10.1029/1998JD100047>.

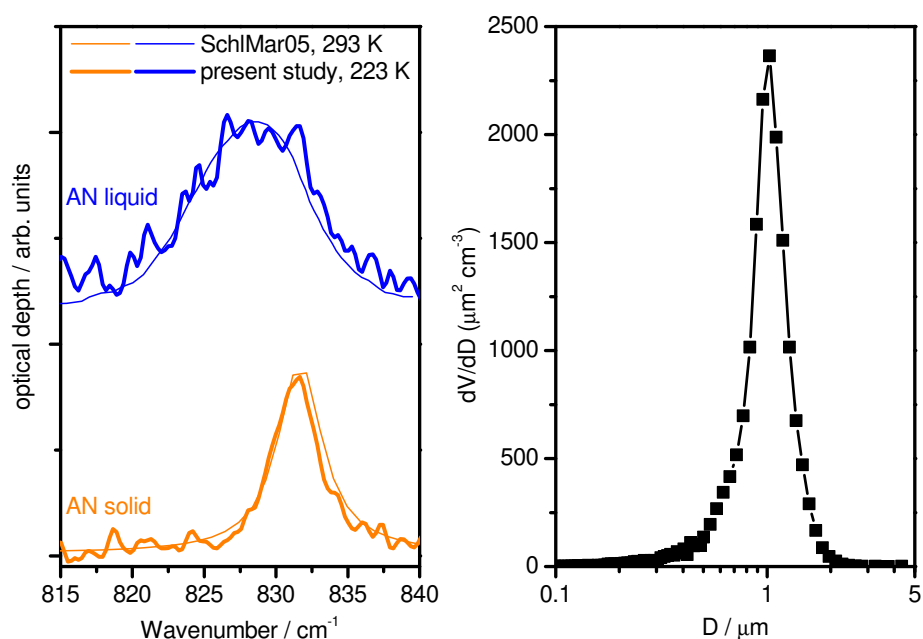
## Supplementary Figures 1–11



Supplementary Figure 1: **Infrared spectra of AN.** The  $\nu_2(\text{NO}_3^-)$  infrared band of AN as observed in laboratory (AIDA) and inside the AMA by the CRISTA satellite instrument [15]. The CRISTA signal with  $1.5\text{ cm}^{-1}$  spectral resolution has been derived from all spectra measured during the flight in August 1997 within a tangent altitude range of 16–18 km,  $20^\circ$ – $50^\circ\text{N}$  and  $30^\circ$ – $180^\circ\text{E}$  (see Methods). The laboratory spectra of optical depth (liquid AN: blue, solid AN: orange) and the satellite radiances (green) are scaled and offset to facilitate their comparison.

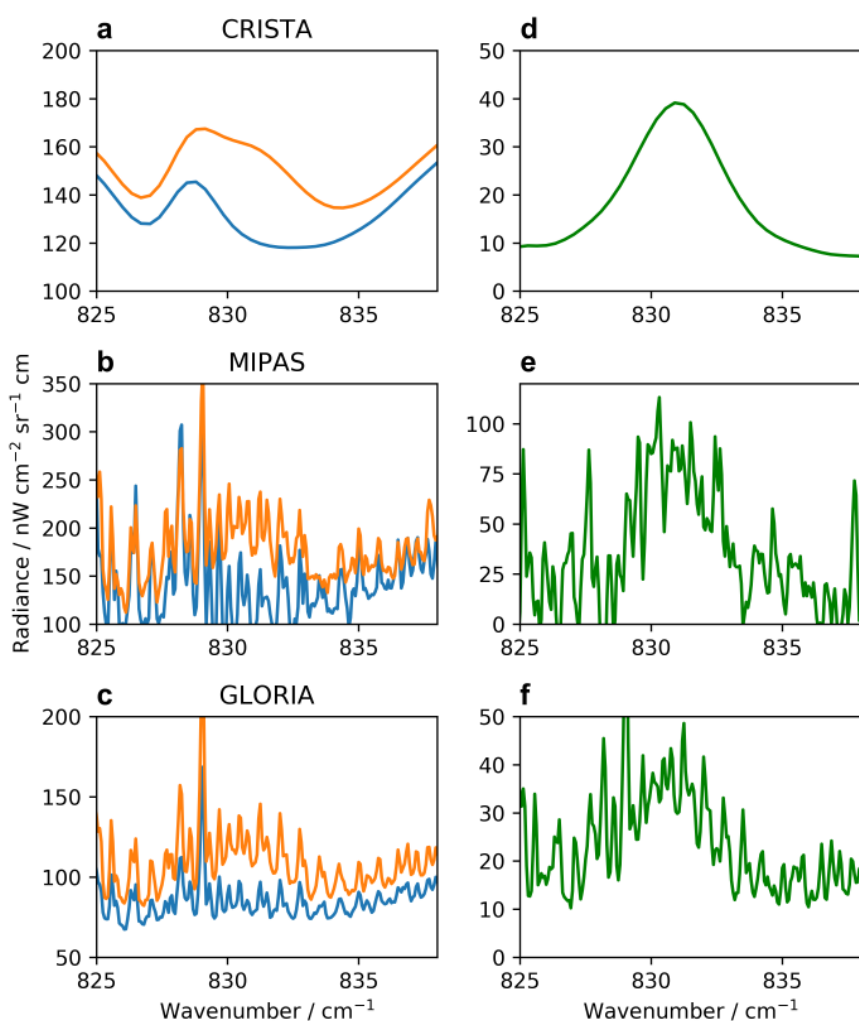


Supplementary Figure 2: **AIDA laboratory spectra of liquid and solid AN particles.** Mid-infrared spectra of aerosol particles composed of AN and mixtures of AN and AS. Top panel: Spectral regime from 6000 to 800  $\text{cm}^{-1}$  (with  $\text{CO}_2$  absorption regime between 2450 and 2150  $\text{cm}^{-1}$  excluded). Bottom panel: Expanded view from 1600 to 800  $\text{cm}^{-1}$ . Spectra A to D were recorded at 223 K in the AIDA chamber, whereas spectrum E, recorded at 293 K, was taken from the literature [1]. All spectra were scaled and offset to facilitate their comparison. See Supplementary discussion for details.

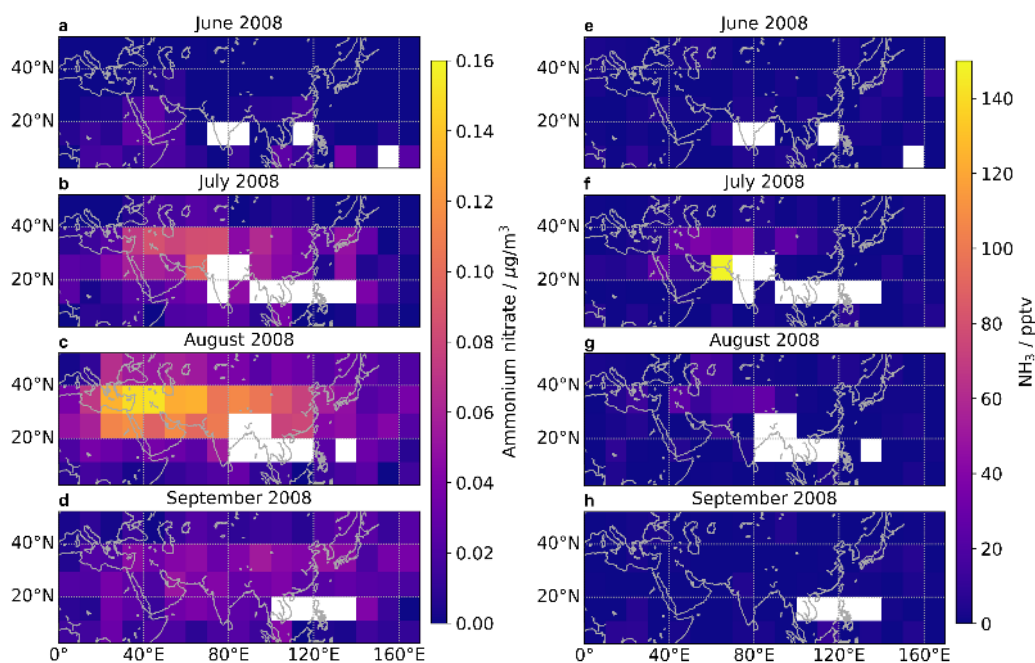


Supplementary Figure 3: **Comparison of laboratory spectra of liquid and solid AN and volume size distribution.** Left panel: Comparison of the  $\nu_2(\text{NO}_3^-)$  infrared absorption mode of liquid and solid AN particles, recorded at 223 K during the present AIDA experiments (expanded view of spectra A and B from Supplementary Fig. 2) and at 293 K during previous aerosol flow-tube experiments (“SchlMar05”, digitized graphs from the inserts in Figs. 2 and 5 of [1]). All spectra were scaled and offset to facilitate their comparison. Right panel: Volume-size distribution of crystalline aerosol particles generated from the 97.1 mol% AN + 2.9 mol% AS bulk solution after injection into the AIDA chamber at 223 K and 22% RH.

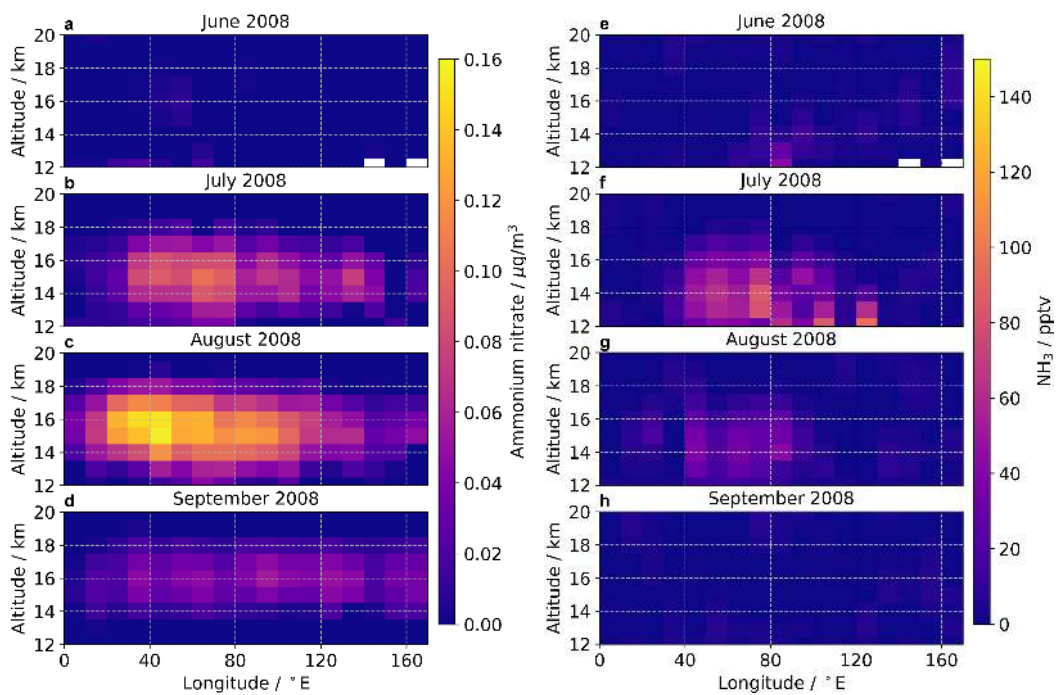




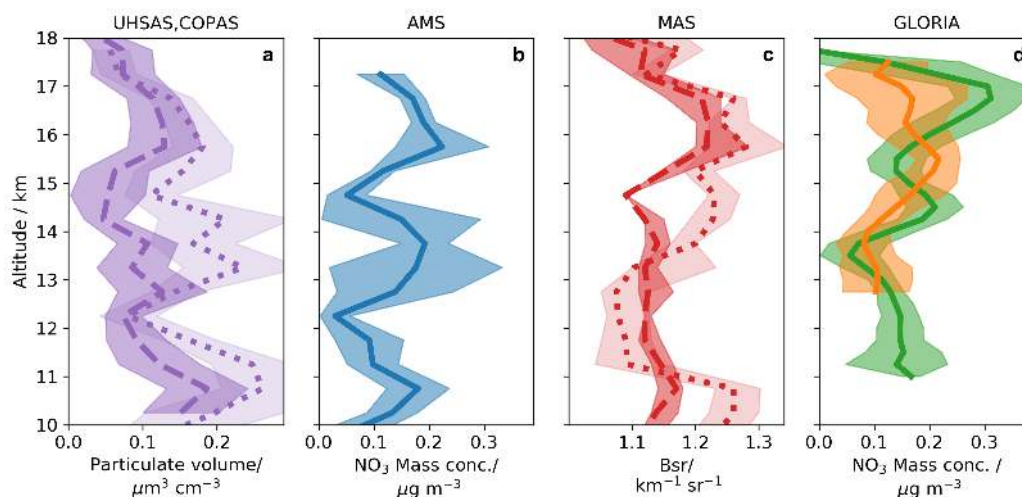
Supplementary Figure 4: **Detection of the  $\nu_2(\text{NO}_3^-)$  infrared band of ammonium nitrate in infrared limb spectra.** Measured spectra with (orange) and without (blue) the spectral band of AN and their difference (green). The spectra have been taken from observations obtained at different locations with high and low concentrations of AN, respectively. **a,d**, CRISTA data are averaged spectra selected over the whole Space Shuttle flight in August 1997 within a tangent altitude range of 16–18 km, 20–50° latitude and 30–180° longitude. **b,e**, MIPAS spectra between 15 km and 16 km tangent altitude from 8 August 2008, 7:15:30 UTC (orange) and 3:52:17 UTC (blue). **c,f**, mean GLORIA spectra from flight 31 July 2017 at tangent altitudes between 16.5 and 16.75 km at 4:15–4:21 UTC (orange) and 3:55–3:59 UTC (blue).



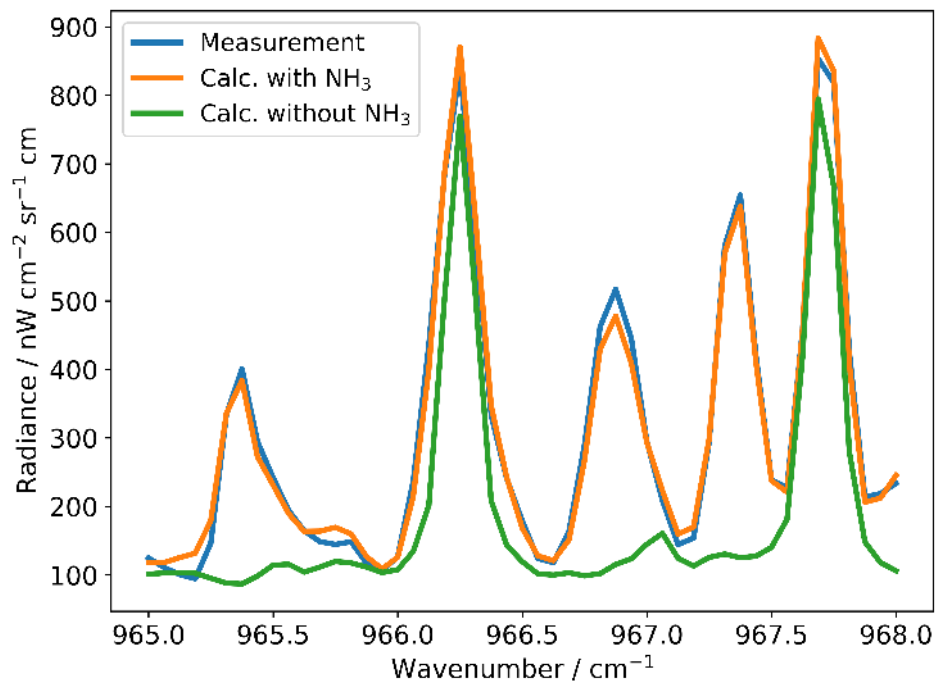
Supplementary Figure 5: **Ammonium nitrate and ammonia observed by MIPAS in the UT during the Asian monsoon 2008.** Monthly mean AN mass concentrations (**a–d**) and  $\text{NH}_3$  volume mixing ratios (**e–h**) at 16 km altitude derived from MIPAS observations from June to September 2008. Data are monthly averages of single retrieved profiles within a  $10^\circ$  latitude  $\times$   $10^\circ$  longitude grid.



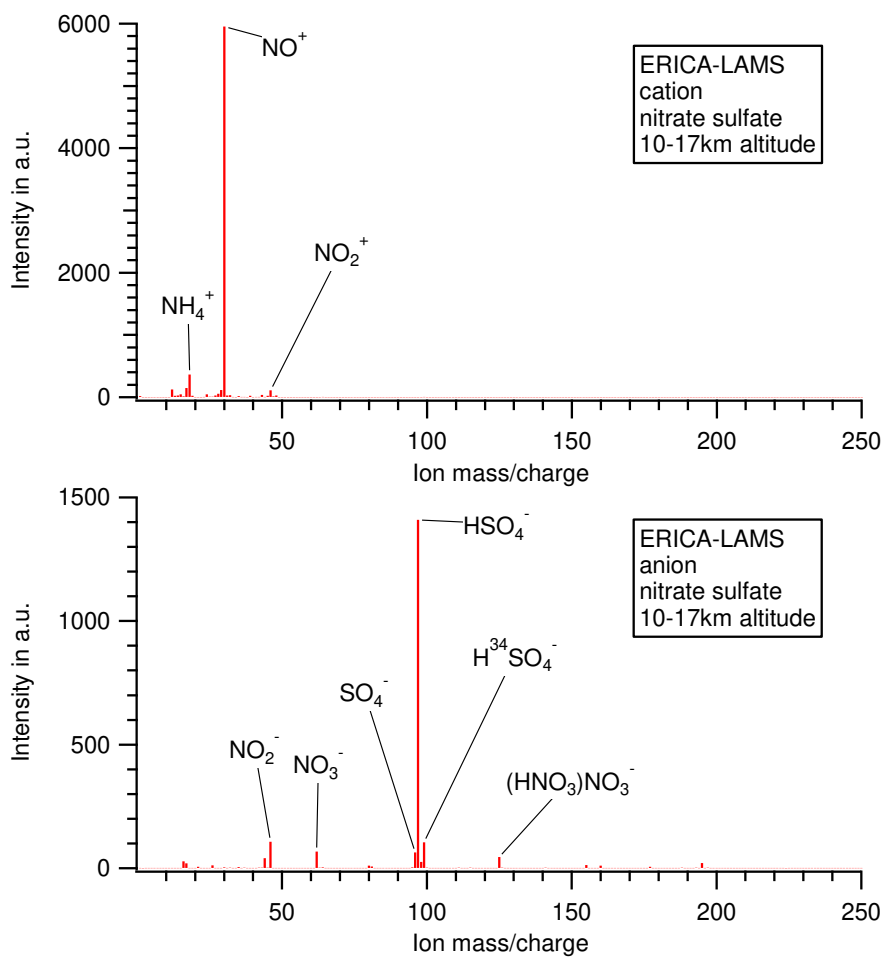
Supplementary Figure 6: **Ammonium nitrate and ammonia observed by MIPAS in the UT during the Asian monsoon 2008.** Monthly mean AN mass concentrations (a–d) and  $\text{NH}_3$  volume mixing ratios (e–h) at  $30\text{--}40^\circ\text{N}$  derived from MIPAS observations from June to September 2008. Data are monthly averages of single profiles within a  $10^\circ$  latitude  $\times$   $10^\circ$  longitude grid.



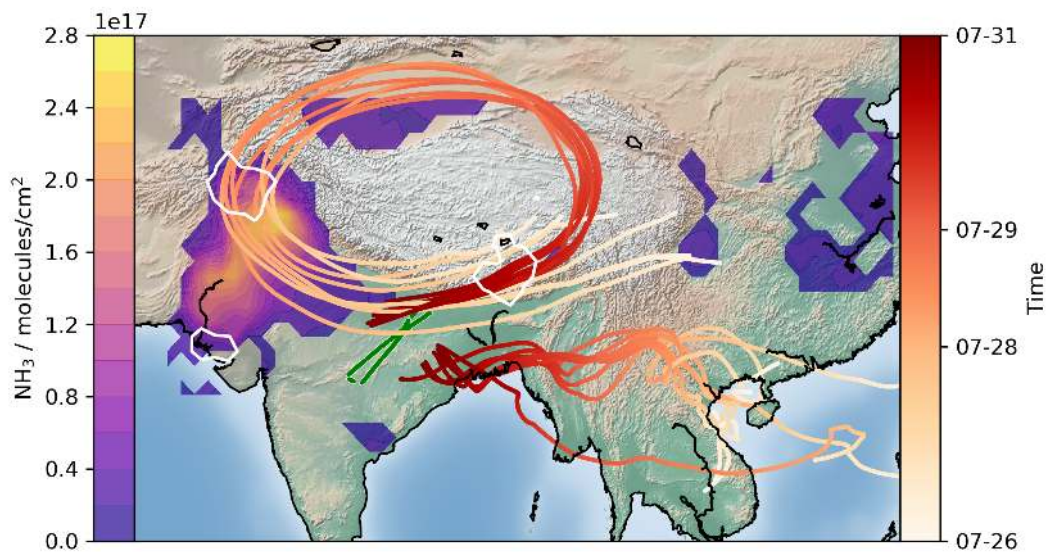
Supplementary Figure 7: **Airborne aerosol observations in the Asian monsoon UT on 31 July 2017.** **a**, UHSAS and COPAS derived aerosol volume density during ascent (dashed) and descent (dotted). **b**, ERICA-AMS particulate  $\text{NO}_3^-$  mass concentrations. **c**, MAS backscatter ratios (Bsr) at 532 nm during ascent (dashed) and descent (dotted). **d**, GLORIA  $\text{NO}_3^-$  mass concentration profiles from AN retrievals. **a–c**, have been obtained during ascent and descent at Kathmandu. The values are averages in vertical bins of 0.25 km. GLORIA data are mean profiles averaged during the flight between 3:50–3:55 UTC (orange) and between 4:05–4:10 UTC (green). Shaded areas indicate 25 and 75 percentiles for MAS and standard deviations in case of the other datasets. For the nitrate content of ERICA-AMS, the uncertainty is estimated to 30%. The estimated uncertainty of the UHSAS and COPAS data is below 30%. The uncertainty of MAS Bsr is estimated to 0.05. The estimated accuracy of the GLORIA data is 30%.



Supplementary Figure 8: **Detection of NH<sub>3</sub> emission lines in GLORIA limb infrared spectra.** Example of a GLORIA spectrum at a tangent height of 13.7 km on 31 July 2017, 4:15 UTC (blue) in comparison to the spectral fit including NH<sub>3</sub> spectral lines (orange) and a calculation without consideration of NH<sub>3</sub> (green). The two strongest lines belong to CO<sub>2</sub>.

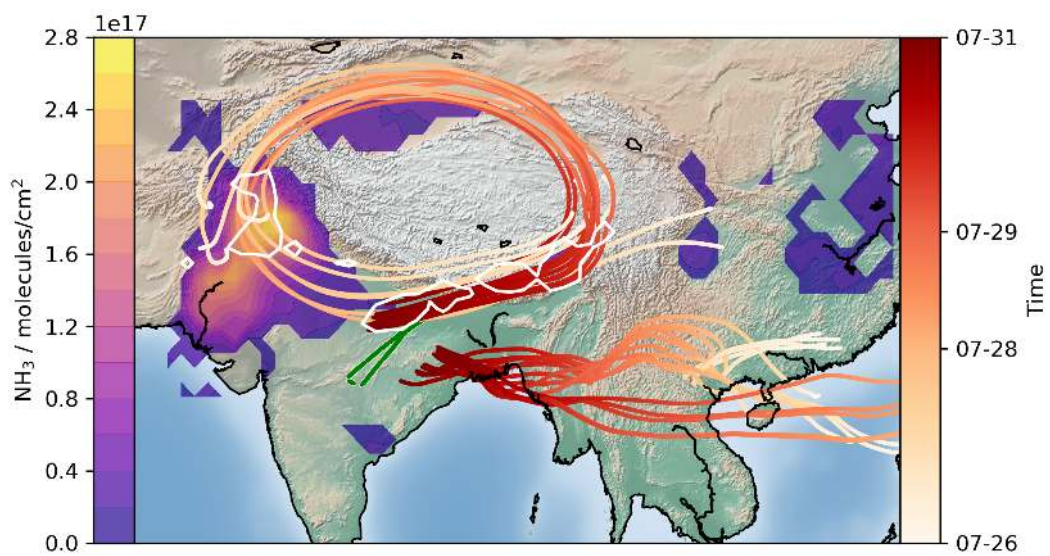


Supplementary Figure 9: **Particles containing nitrate and sulfate.** Average single particle mass spectra taken by ERICA-LAMS during the whole StratoClim campaign with simultaneously present spectral lines of sulfate and nitrate ions indicating that the individual particles of this category contain both, sulfate and nitrate components.



Supplementary Figure 10: **The origin of high NH<sub>3</sub> concentrations in the UT.** Exemplary subsets of backward TRACZILLA trajectories starting at GLORIA observations with enhanced NH<sub>3</sub> concentrations (SW-bound flight leg) and at no NH<sub>3</sub> enhancement (NE-bound leg) on 31 July 2017. The trajectories are colour-coded according to time. White contour lines highlight regions where the density of convective events, for the NH<sub>3</sub>-enhancement trajectories release, is larger than 0.5%. This quantity is computed as the ratio, on a 1° latitude × 1° longitude grid, of the number of encountered convective events with respect to the total number of released trajectories. Mean IASI column amounts of NH<sub>3</sub> for the time period 26–30 July 2017 are indicated by the colours of the left colour bar. IASI measurements less than 5% of the maximum value are not plotted. The aircraft flight path is shown as a green line.





Supplementary Figure 11: **The origin of high  $\text{NH}_3$  concentrations in the UT.** Same as Supplementary Fig. 10, but with trajectory data from the ATLAS model.